

1 Effects of organic coating on the nitrate formation by suppressing the N₂O₅ heterogeneous
2 hydrolysis: A case study during wintertime in Beijing-Tianjin-Hebei (BTH)

3
4 Lang Liu^{1,4}, Jiarui Wu¹, Suixin Liu¹, Xia Li¹, Jiamao Zhou¹, Tian Feng¹, Yang Qian³, Junji Cao^{1,2}, Xuexi Tie¹,
5 Guohui Li^{1,2*}
6

7 ¹Key Lab of Aerosol Chemistry and Physics, SKLLQG, Institute of Earth Environment, Chinese Academy of
8 Sciences, Xi'an, China

9 ²CAS Center for Excellence in Quaternary Science and Global Change, Xi'an, China

10 ³State Key Laboratory of Environmental Criteria and Risk Assessment & Environmental Standards Institute,
11 Chinese Research Academy of Environmental Sciences, Beijing, China

12 ⁴University of Chinese Academy of Sciences, Beijing, China
13

14 *Correspondence to:* Guohui Li (ligh@ieecas.cn)
15
16

17 **Abstract:** Although stringent emission mitigation strategies have been carried out since 2013
18 in Beijing-Tianjin-Hebei (BTH), China, heavy haze with high levels of fine particulate matter
19 (PM_{2.5}) still frequently engulfs the region during wintertime and the nitrate contribution to
20 PM_{2.5} mass has progressively increased. The N₂O₅ heterogeneous hydrolysis is the most
21 important pathway of the nitrate formation at nighttime. In the present study, the WRF-Chem
22 model is applied to simulate a heavy haze episode from 10 to 27 February 2014 in BTH to
23 evaluate contributions of the N₂O₅ heterogeneous hydrolysis to nitrate formation and effects
24 of organic coating. The model generally performs reasonably well in simulating
25 meteorological parameters, air pollutants and aerosol species against observations in BTH.
26 The N₂O₅ heterogeneous hydrolysis with all the secondary organic aerosol assumed to be
27 involved in coating considerably improves the nitrate simulations compared to the
28 measurements in Beijing. On average, organic coating decreases nitrate concentrations by 8.4%
29 in BTH during the episode, and the N₂O₅ heterogeneous hydrolysis with organic coating
30 contributes about 30.1% of nitrate concentrations. Additionally, the reaction also plays a
31 considerable role in the heavy haze formation, with a PM_{2.5} contribution of about 11.6% in
32 BTH. Sensitivity studies also reveal that future studies need to be conducted to predict the
33 organic aerosol hygroscopicity for accurately representing the organic coating effect on the
34 N₂O₅ heterogeneous hydrolysis.
35
36
37
38
39

40 **1 Introduction**

41 Within recent decades, China has been suffering from pervasive and persistent haze
42 pollution caused by elevated levels of fine particulate matters (PM_{2.5}), particularly in
43 Beijing-Tianjin-Hebei (BTH) (Guo et al., 2014; Gao et al., 2016; Wang et al., 2016).
44 Numerous studies have revealed that the inorganic aerosols, including nitrate, sulfate and
45 ammonium, are the most abundant component of PM_{2.5} during haze pollution episodes in
46 BTH, and that the evolution of the haze pollution is characterized by the formation of
47 substantial amounts of sulfate and nitrate (Sun et al., 2013; Zhang et al., 2013; Zhao et al.,
48 2013; Sun et al., 2015). Since 2013, several aggressive emission control strategies have been
49 implemented in China, including desulfurization and dedusting for coal combustion, vehicle
50 restriction and executing stringent emission standards in the key industries (Tao et al., 2017).
51 However, the control of emissions of nitrate gaseous precursors does not seem to be effective,
52 since many observations have shown that the nitrate aerosol concentration has progressively
53 increased in recent several years (Zhang et al., 2012; Sun et al., 2015; Zhang et al., 2015; Tao
54 et al., 2017).

55 In the atmosphere, nitrate aerosol is formed via nitrous acid (HNO₃) to balance the
56 inorganic cations in the aerosol phase. HNO₃ is produced through four pathways (Kim et al.,
57 2014): (1) the reaction of OH and NO₂ (main gas phase pathway and usually considered as
58 the daytime pathway because the OH radical is severely limited at night due to lack of O₃ and
59 peroxide photolysis), (2) NO₃ radical reaction with hydrocarbons, (3) aqueous reaction of
60 NO₃ radical to form HNO₃, and (4) NO₃ conversion to N₂O₅ with subsequently
61 heterogeneous chemical conversion to form HNO₃. The last pathway is referred to as the
62 most important pathway during nighttime, since both NO₃ and N₂O₅ are photolytically liable,
63 or even under heavy haze situation with weak sunlight and high relative humidity (RH)
64 (Brown et al., 2016).

65 The heterogeneous hydrolysis of N_2O_5 on the surface of deliquescent aerosols to form
66 HNO_3 is quantified by the reaction probability ($\gamma_{N_2O_5}$) (Bertram and Thornton, 2009; Chen et
67 al., 2018; Davis et al., 2008; Riemer et al., 2003). $\gamma_{N_2O_5}$ has been measured by previous
68 laboratory experiments, dependent on particulate chemical composition, RH, temperature,
69 aerosol surface area and water content (Chang et al., 2011), and in the order of 10^{-2} (Zheng et
70 al., 2015). In modeling studies, various parameterizations of $\gamma_{N_2O_5}$ are used to simulate the
71 nitrate formation. Dentener and Crutzen (1993) have first used 0.1 as the representative
72 $\gamma_{N_2O_5}$ in a three-dimensional global model. Riemer et al. (2003) have developed a $\gamma_{N_2O_5}$
73 parameterization on the surface of aerosols containing sulfate and nitrate (hereafter referred
74 as to Riemer03), which has widely been used and further improved in air quality models.
75 Davis et al. (2008) have implemented a $\gamma_{N_2O_5}$ parameterization on the surface of particles
76 containing sulfate, nitrate, ammonium, as a function of RH, temperature and phase state, to
77 improve simulations of N_2O_5 hydrolysis. Bertram and Thornton (2009) have developed a
78 parameterization to consider the influence of chloride salts on $\gamma_{N_2O_5}$ as a function of RH.

79 The coating of particles by organic materials has been reported to inhibit N_2O_5 uptake
80 (Anttila et al., 2006), and suggested as a possible explanation for field observations of
81 suppressed N_2O_5 uptake (Brown et al., 2006). Evans and Jacob (2005) have incorporated a
82 $\gamma_{N_2O_5}$ parameterization on surfaces of sulfate particles as a function of RH and temperature
83 into the GEOS-CHEM model, including the effects of dust, sea salt, sulfate, elemental carbon
84 and organic carbon but ignoring the nitrogen-containing species. Riemer et al. (2009) have
85 developed a N_2O_5 uptake parameterization (Riemer09) based on the laboratory results of
86 Anttila et al. (2006), which combines the nitrogen-containing and organic effects on N_2O_5
87 hydrolysis. The parameterization has been used to estimate the maximum effect of organic
88 coating by assuming that all available secondary organic compounds (SOC) contribute to the
89 coating in a 3-D model. The results show that SOC could suppress N_2O_5 uptake significantly,

90 reducing particulate nitrate concentrations by up to 90%. Lowe et al. (2015) have further
91 combined the organic coating and chloride salts effects on $\gamma_{N_2O_5}$ in the WRF-Chem model.
92 Most recently, Chen et al. (2018) have developed a new $\gamma_{N_2O_5}$ parameterization with respect
93 to RH, temperature, and aerosol composition, showing that organic coating effect on $\gamma_{N_2O_5}$
94 is not as important as expected over western and central Europe. However, there is still a lack
95 of modeling studies focused on the effect of organic coating on $\gamma_{N_2O_5}$ and particulate nitrate
96 formation in China. Wang et al. (2017) have evaluated the potential particulate nitrate
97 formation through the N_2O_5 hydrolysis reaction without considering the organic coating
98 effect during a haze pollution episode in Beijing, and found that the observed nitrate
99 concentration ($20.6 \mu\text{g m}^{-3}$ on average) is lower than the assessment ($57.0 \mu\text{g m}^{-3}$ on average).
100 Considering the high organic aerosol concentration and increasing trend of particulate nitrate
101 during haze days in BTH, it is imperative to assess the effect of organic coating on N_2O_5
102 hydrolysis and its consequent contribution to the nitrate formation.

103 In the present study, based on Riemer09 parameterization, the contribution of the
104 organic coating effect on N_2O_5 hydrolysis to the nitrate formation is investigated using the
105 WRF-Chem model. The model configuration and methodology are described in Section 2.
106 Results and sensitivity studies are presented in Section 3. Discussion and summary are given
107 in section 4.

108

109 **2 Model and Methodology**

110 **2.1 WRF-Chem model and configuration**

111 A modified version of the WRF-Chem model (Grell et al., 2005) is used in this study,
112 which is developed by Li et al. (2010; 2011a; 2011b; 2012) at the Molina Center for Energy
113 and the Environment. A new flexible gas phase chemical module has been developed and
114 implemented into the version of the WRF-Chem model, which can be utilized with different

115 chemical mechanisms, including CBIV, RADM2, and SAPRC. The gas-phase chemistry is
116 solved by an Eulerian backward Gauss-Seidel iterative technique with a number of iterations,
117 inherited from NCAR-HANK (Hess et al., 2000). In the study, the SAPRC99 chemical
118 mechanism is used based on the available emission inventory. For the aerosol simulations, the
119 CMAQ/models3 aerosol module (AERO5) developed by US EPA has incorporated into the
120 model (Binkowski and Roselle, 2003). Briefly, the wet deposition uses the method in the
121 CMAQ module and the dry deposition of chemical species is parameterized following
122 Wesely (1989). The photolysis rates are calculated using the Fast Tropospheric Ultraviolet
123 and Visible Radiation Model (FTUV; Tie et al., 2003; Li et al., 2005), with the aerosol and
124 cloud effects on the photochemistry (Li et al., 2011a).

125 ISORROPIA (version 1.7) is used to predict the thermodynamic equilibrium between the
126 ammonia-sulfate-nitrate-chloride-water aerosols and their gas phase precursors of
127 H₂SO₄-HNO₃-NH₃-HCl-water vapor. It is worth noting that the most recent extension of
128 ISORROPIA, known as ISORROPIA II, has incorporated a larger number aerosol species
129 (Ca, Mn, K salts) and is designed to be a superset of ISORROPIA (Fountoukis and Nenes,
130 2007). Considering that crustal species are not considered in the study, ISORROPIA (version
131 1.7) is still used to calculate inorganic components and ISORROPIA II is imperative to be
132 incorporated into the WRF-Chem model in future studies. In addition, a parameterization of
133 sulfate heterogeneous formation involving aerosol liquid water (ALW) has been developed
134 and implemented into the model, which has successfully reproduced the observed rapid
135 sulfate formation during haze days (Li et al., 2017). The sulfate heterogeneous formation
136 from SO₂ is parameterized as a first order irreversible uptake by ALW surfaces, with a
137 reactive uptake coefficient of 0.5×10^{-4} assuming that there is enough alkalinity to maintain
138 the high iron-catalyzed reaction rate.

139 The OA module is based on the VBS approach with aging and detailed information can

140 be found in Li et al. (2011b). The POA components from traffic-related combustion and
141 biomass burning are represented by nine surrogate species with saturation concentrations (C^*)
142 ranging from 10^{-2} to $10^6 \mu\text{g m}^{-3}$ at room temperature (Shrivastava et al., 2008), and assumed
143 to be semi-volatile and photochemically reactive (Robinson et al., 2007). The SOA formation
144 from each anthropogenic or biogenic precursor is calculated using four semi-volatile VOCs
145 with effective saturation concentrations of 1, 10, 100, and $1000 \mu\text{g m}^{-3}$ at 298 K. The SOA
146 formation via the heterogeneous reaction of glyoxal and methylglyoxal is parameterized as a
147 first-order irreversible uptake by aerosol particles with an uptake coefficient of 3.7×10^{-3}
148 (Liggio et al., 2005; Zhao et al., 2006; Volkamer et al., 2007). The OA module has reasonably
149 reproduced the POA and SOA concentration against measurements, and detailed model
150 performance can be found in Li et al. (2011b), Feng et al. (2016), and Xing et al. (2019).

151 The anthropogenic emission inventory with a horizontal resolution of 6 km is developed
152 by Zhang et al. (2009), with the base year of 2013, including industry, transportation, power
153 plant, residential and agriculture sources. The Model of Emissions of Gases and Aerosols
154 from Nature (MEGAN) is used to calculate the biogenic emissions online (Guenther et al.,
155 2006).

156 A heavy haze episode from 10 to 27 February 2014 in BTH is simulated in association
157 with the field observation of air pollutants and secondary inorganic aerosols. Detailed model
158 configuration can be found in Table 1 and the simulation domain is presented in Figure 1.

159 **2.2 Parameterization of the heterogeneous hydrolysis of N_2O_5**

160 The reaction of N_2O_5 heterogeneous hydrolysis on the surface of deliquescent aerosols
161 to form HNO_3 can be represented as:



163 This reaction is usually implemented into air quality transport models as a first order loss:

$$164 \quad \frac{\partial[\text{N}_2\text{O}_5]}{\partial t} = -k_{\text{N}_2\text{O}_5} \cdot [\text{N}_2\text{O}_5] \quad (\text{Eq. 2})$$

165 $[N_2O_5]$ represents the N_2O_5 concentration in the atmosphere. The loss rate constant, $k_{N_2O_5}$, is
166 parameterized in the following way:

$$167 \quad k_{N_2O_5} = \frac{1}{4} \cdot c_{N_2O_5} \cdot S \cdot \gamma_{N_2O_5} \quad (\text{Eq. 3})$$

168 Where $c_{N_2O_5}$ is the average molecular velocity of N_2O_5 , and S is the available aerosol
169 surface area density.

170 In this study, the parameterization of $\gamma_{N_2O_5}$ follows Riemer03 and Riemer09. In the
171 parameterization, the primary emission compounds such as element carbon, insoluble organic
172 matter (most part of POA), insoluble inorganic and mineral dust particles are assumed to
173 serve as a nucleus of aerosols. Condensation of soluble chemical components and further
174 water vapor on the surface of the nucleus forms an aqueous layer. The nucleus and the
175 aqueous layer are assumed as unified “core” (aqueous core) in Riemer03 and Riemer09
176 parameterizations. In Riemer03 parameterization, soluble inorganic components including
177 sulfate and nitrate are taken into consideration for suppressing the N_2O_5 heterogeneous
178 hydrolysis uptake in the aqueous core, and the parameterization of $\gamma_{N_2O_5}$ is defined as:

$$179 \quad \gamma_{N_2O_5} = f \cdot \gamma_1 + (1 - f) \cdot \gamma_2 \quad (\text{Eq. 4})$$

180 with $\gamma_1 = 0.02$ and $\gamma_2 = 0.002$, and f is defined as:

$$181 \quad f = \frac{m_{SO_4^{2-}}}{m_{SO_4^{2-}} + m_{NO_3^-}} \quad (\text{Eq. 5})$$

182 $m_{SO_4^{2-}}$ and $m_{NO_3^-}$ are the aerosol mass concentrations of soluble sulfate and nitrate.

183 In Riemer09 parameterization, unreactive organic layers are further considered for the
184 suppression of N_2O_5 hydrolysis by covering the aqueous core. Organic layers may be formed
185 by secondary organic aerosols, and such layers may consist of a single layer of molecules
186 (monolayered coatings) or of several molecule layers (multilayered coatings) on the surface
187 of the aqueous core. These organic layers are assumed as organic “coating” (shell) in the
188 Riemer09 parameterization. The resistor scheme to calculate $\gamma_{N_2O_5}$ in Riemer09

189 parameterization is parameterized as follows:

$$190 \quad \frac{1}{\gamma_{N_2O_5}} = \frac{1}{\gamma_{N_2O_5,core}} + \frac{1}{\gamma_{N_2O_5,coat}} \quad (\text{Eq. 6})$$

191 where $\gamma_{N_2O_5,core}$ is the reaction probability of the aqueous core which is calculated using Eq.
192 4, and $\gamma_{N_2O_5,coat}$ is the pseudo-reaction probability of the organic coating calculated by the
193 following formulation:

$$194 \quad \gamma_{N_2O_5,coat} = \frac{4 \cdot R \cdot T \cdot H_{org} \cdot D_{org} \cdot R_c}{c_{N_2O_5} \cdot \ell \cdot R_p} \quad (\text{Eq. 7})$$

195 Where R is the universal gas constant, T is temperature, H_{org} is the Henry's law constant for
196 N_2O_5 in the organic coating, and D_{org} is the diffusion coefficient for N_2O_5 in the organic
197 coating. H_{org} and D_{org} depend on the physicochemical properties of the compounds
198 comprising the organic coating. In the Riemer09 scheme, $H_{org} \cdot D_{org}$ is defined as
199 $0.03 \cdot H_{aq} \cdot D_{aq}$. H_{aq} is the Henry's law constant of N_2O_5 for the aqueous phase ($H_{aq} = 5000$
200 $M \text{ atm}^{-1}$) and D_{aq} is the diffusion coefficient of N_2O_5 in the aqueous phase ($D_{aq} = 10^{-9} \text{ m}^2$
201 s^{-1}). R_p , R_c , and ℓ are the radius of the particle, radius of the inorganic core, and thickness
202 of the coating, respectively. R_p , R_c , and ℓ are calculated as follows:

$$203 \quad R_p = R_c + \ell \quad (\text{Eq. 8})$$

$$204 \quad \ell = R_p \cdot (1 - \beta^{\frac{1}{3}}) \quad (\text{Eq. 9})$$

$$205 \quad \beta = \frac{V_{inorg}}{V_{inorg} + V_{org}} \quad (\text{Eq. 10})$$

206 Where V_{inorg} and V_{org} are the volume of inorganic and organic materials, respectively.

207 **2.3 Statistical methods for model evaluation**

208 In this study, the mean bias (MB), root mean square error (RMSE), the index of
209 agreement (IOA), mean fractional bias (MFB) and mean fractional error (MFE) are used to
210 evaluate the model performance in simulating air pollutants.

$$211 \quad \text{MB} = \frac{1}{N} \sum_{i=1}^N (P_i - O_i) \quad (\text{Eq. 11})$$

$$212 \quad \text{RMSE} = \left[\frac{1}{N} \sum_{i=1}^N (P_i - O_i)^2 \right]^{\frac{1}{2}} \quad (\text{Eq. 12})$$

$$213 \quad \text{IOA} = 1 - \frac{\sum_{i=1}^N (P_i - O_i)^2}{\sum_{i=1}^N (|P_i - \bar{O}| + |O_i - \bar{O}|)^2} \quad (\text{Eq. 13})$$

$$214 \quad \text{MFB} = \frac{1}{N} \sum_{i=1}^N \frac{P_i - O_i}{(P_i + O_i)/2} \quad (\text{Eq. 14})$$

$$215 \quad \text{MFE} = \frac{1}{N} \sum_{i=1}^N \frac{|P_i - O_i|}{(P_i + O_i)/2} \quad (\text{Eq. 15})$$

216 Where P_i and O_i are the simulated and observed variables, respectively. N is the total
 217 number of the simulations for comparisons, and \bar{O} donates the average of the observation.
 218 The IOA ranges from 0 to 1, with 1 showing a perfect agreement of the simulation with the
 219 observation.

220 **2.4 Air pollutants observations**

221 Simulations are compared to available meteorological and air pollutants observations to
 222 evaluate the model performance. The meteorological parameters including temperature, RH,
 223 wind speed and direction are obtained from the website <http://www.meteomanz.com>. The
 224 hourly observations of PM_{2.5}, O₃, SO₂, NO₂, and CO concentrations are released by China
 225 National Environmental Monitoring Center and can be downloaded from the website
 226 <http://106.37.208.233:20035>.

227 Additionally, hourly OC and EC concentrations are measured using a thermal/optical
 228 reflectance carbon analyzer (OCEC RT-4, Sunset Lab, USA) at Chinese Research Academy
 229 of Environmental Sciences (CRAES, 40.04°N, 116.40°E) in Beijing (Wei et al., 2014; Liu et
 230 al., 2018). Hourly sulfate, nitrate, ammonium, and other inorganic ions are sampled and
 231 analyzed by ion chromatography (URG 9000S, Thermo Fisher Scientific, USA).

232 The OC/EC ratio approach is used to derive the SOA mass concentrations from EC and
 233 OC filter measurements as follows (Strader, 1999; Cao et al., 2004):

$$234 \quad \text{POC} = \text{EC} \times \left(\frac{\text{POC}}{\text{EC}} \right) \quad (\text{Eq. 16})$$

235
$$SOC = OC - POC \quad (\text{Eq. 17})$$

236
$$SOA = SOC \times \left(\frac{SOA}{SOC}\right) \quad (\text{Eq. 18})$$

237 Where POC and SOC are the primary OC and secondary OC, respectively. In the present
238 study, $\frac{POC}{EC}$ and $\frac{SOA}{SOC}$ are assumed to be 2.4 and 1.6, respectively, based on the previous
239 studies (Cao et al., 2007; Aiken et al., 2008; Yu et al., 2009) and detailed information about
240 the approach can be found in Feng et al. (2016). It is worth noting that those assumed $\frac{POC}{EC}$
241 and $\frac{SOA}{SOC}$ could potentially affect the model-measurement comparisons.

242

243 **3 Results and discussion**

244 **3.1 Synoptic conditions during the wintertime of 2014**

245 Based on the NCEP FNL reanalysis data (<https://rda.ucar.edu/datasets/ds083.2>), we have
246 initially performed the analysis of synoptic conditions using the wind, temperature, relative
247 humidity, and geopotential height fields at 500hPa and 850hPa averaged from 10 to 27
248 February 2014 over China, respectively (Figure 2). At 500hPa, flat westerly winds prevail
249 over BTH and its surrounding area, indicating a stagnant atmospheric circulation conditions
250 (Figure 2a). Moreover, the flat isotherm distribution is similar to that of the isobar at 500hpa,
251 showing that there is no obvious exchange of cold and warm air masses, which together with
252 the flat westerly leads to the weak turbulent mixing in the vertical direction and the stable
253 weather condition (Figure 2b). At 850hPa, the southeast coastal areas of China are controlled
254 by the anti-cyclone whose center locates over the South China Sea (Figure 2c). In the eastern
255 China influenced by the anti-cyclone, the weak southerly wind prevails over the BTH and its
256 surrounding regions, providing a favorable condition for stagnant weather conditions and
257 further the formation of air pollution. With the prevailing southerly wind, the warm and
258 humid air flow and the polluted air mass are subject to being transported from south to north,

259 aggravating the air pollution in BTH. In addition, high relative humidity conditions facilitate
260 the heterogeneous reactions for the secondary aerosol formation (Figure 2d).

261 **3.2 Model performance**

262 In order to quantify effects of the N_2O_5 heterogeneous hydrolysis and organic coating on
263 the nitrate formation, three experiments have been performed in the study. In the base case,
264 Riemer09 parameterization is used to take into consideration the organic coating effect on the
265 N_2O_5 heterogeneous hydrolysis by assuming that all the SOA is involved in coating (hereafter
266 referred to as B-case). In the first sensitivity case, the contribution of N_2O_5 heterogeneous
267 hydrolysis to the nitrate formation is not considered (hereafter referred to as H0-case); In the
268 second sensitivity case, the organic coating effect is not considered in Riemer09
269 parameterization (hereafter referred to as C0-case). The simulation results in the B-case are
270 compared to observations in BTH.

271 3.2.1 Meteorological parameters simulations in Beijing

272 Considering that the meteorological conditions play a crucial role in air pollution
273 simulations, which determine accumulation or dispersion of pollutants, verifications are first
274 performed for the simulations of meteorological fields. Figure 3 presents the temporal profile
275 of the simulated and observed temperature, RH, wind speed, and wind direction averaged
276 over 12 meteorological sites in Beijing from 10 to 27 February 2014. The WRF-Chem model
277 reproduces well the temporal variation of the surface temperature during the whole episode.
278 The MB and RMSE is -0.2 and 1.7°C, and the IOA reaches 0.94, indicating good agreement
279 of the simulations with observations (Table 2). The simulated temporal RH variations are also
280 well consistent with observations, with the MB, RMSE and IOA of 2.6%, 10.9% and 0.89,
281 respectively. In addition, the model reasonably well tracks the temporal variations of the
282 surface wind, with IOAs of 0.73 and 0.66 for the wind speed and direction, respectively.

283 3.2.2 Air pollutants simulations in BTH

284 Figure 4 shows the relationship between observed and simulated mass concentrations of
285 $PM_{2.5}$, O_3 , SO_2 , NO_2 , and CO in Beijing, Tianjin, and Hebei from 10 to 27 February 2014.
286 The correlation coefficient (R) of $PM_{2.5}$ mass concentrations between observations and
287 simulations in Beijing, Tianjin, and Hebei is 0.83, 0.80, and 0.90, respectively, indicating a
288 good performance of the WRF-Chem model in simulating the $PM_{2.5}$ concentration in BTH.
289 The correlation of O_3 and NO_2 mass concentrations between observations and simulations is
290 not as good as that of $PM_{2.5}$ concentrations in BTH, with the R between 0.6 and 0.8.
291 Apparently, the R of SO_2 simulations with observations show that the WRF-Chem model still
292 has difficulties in well simulating SO_2 concentrations in BTH, particularly in Hebei. Except
293 uncertainties from SO_2 emissions, such as source intensities and distributions, diurnal profiles,
294 et al., the bias of simulated wind fields also substantially influences the SO_2 simulation (Bei
295 et al., 2017). Particularly, SO_2 is principally emitted by the point source, including the power
296 plants and agglomerated industrial zones, so the SO_2 simulations is more sensitive to the
297 wind field simulation uncertainties. In terms of R, the SO_2 simulations in Beijing and Tianjin
298 is better than those in Hebei, indicating that the SO_2 emissions in Beijing and Tianjin are
299 generally determined by area sources, i.e., the residential living, but the point source
300 dominates the SO_2 concentration in Hebei. Considering the long-life time of CO in the
301 atmosphere, the CO simulation is decided by its emission and the meteorological fields. The
302 R of CO simulations with observations in BTH ranges from around 0.6 to 0.7, showing that
303 the CO emissions used in the study and simulated meteorological fields are generally
304 reasonable.

305 Figure 5 presents the diurnal profiles of simulated and observed $PM_{2.5}$, O_3 , NO_2 , SO_2 ,
306 and CO mass concentrations averaged over all ambient monitoring stations in BTH during
307 the simulated episode. The WRF-Chem model well reproduces the diurnal variations of the
308 $PM_{2.5}$ mass concentrations against observations in BTH. The MB and RMSE is -6.3 and

309 27.6 $\mu\text{g m}^{-3}$, respectively, and the IOA is 0.96. The model generally well replicates the haze
310 developing stage, but fails to capture the observed spikes of PM_{2.5} mass concentrations,
311 which might be caused by the uncertainty of the simulated meteorological fields or irregular
312 air pollutants emissions (Bei et al., 2017). The simulated O₃ diurnal variations are in good
313 agreement with observations, with the MB and IOA of 1.4 $\mu\text{g m}^{-3}$ and 0.91, respectively. The
314 model tracks well the observed diurnal variations of NO₂ mass concentrations with an IOA of
315 0.92, but it slightly overestimates NO₂ concentrations compared to observations with a MB of
316 6.6 $\mu\text{g m}^{-3}$. However, during nighttime, the model overestimation is considerable, which is
317 perhaps due to the model biases in modeling nighttime PBL. Although the model reasonably
318 yields the variation trend of the observed SO₂ concentration, with an IOA of 0.85, the
319 dispersion of the simulated SO₂ concentration is rather large, with a RMSE of 27.8 $\mu\text{g m}^{-3}$. In
320 addition, the model overestimates the SO₂ concentration compared to observations, and the
321 MB is 7.6 $\mu\text{g m}^{-3}$, which might be mainly caused by the emission inventory that has
322 undergone noticeable changes since implementation of emission control strategies in 2013 in
323 BTH. The model performs well in simulating CO diurnal variations against observations,
324 with the MB and IOA of 0.2 $\mu\text{g m}^{-3}$ and 0.90, respectively.

325 Figure 6 presents the distributions of simulated and observed near-surface mass
326 concentrations of PM_{2.5}, O₃, NO₂, and SO₂ along with the predicted wind fields averaged
327 during the episode. Generally, the simulated wind in BTH is weak during the episode and the
328 southerly wind prevails, well corresponding to the synoptic situation at 850hPa and 500hPa,
329 which is favorable for the accumulation of air pollutants. The observed PM_{2.5} concentrations
330 are more than 115 $\mu\text{g m}^{-3}$ on average, showing that BTH suffers from heavy haze pollution
331 (Figure 6a). The model generally well reproduces the spatial distribution of PM_{2.5}
332 concentrations against observations, with the PM_{2.5} concentration exceeding 150 $\mu\text{g m}^{-3}$ in
333 the plain area of BTH. The simulated and observed O₃ mass concentrations are less than 50

334 $\mu\text{g m}^{-3}$ in the plain area of BTH, and in several megacities, including Beijing, Tianjin,
335 Baoding, and Shijiazhuang, the O_3 concentrations are less than $30 \mu\text{g m}^{-3}$ (Figure 6b). The
336 low O_3 concentrations during the episode are generally caused by the weak insolation during
337 wintertime, which is unfavorable for photochemical reactions, and the titration due to high
338 NO_x emissions in BTH (Figure 6c). The simulated NO_2 concentrations are generally more
339 than $40 \mu\text{g m}^{-3}$, consistent with the observations at monitoring sites in BTH. The simulated
340 and observed SO_2 mass concentrations in cities or their surrounding areas are still rather high,
341 exceeding $50 \mu\text{g m}^{-3}$ (Figure 6d). Elevated SO_2 concentrations in BTH during wintertime are
342 to some degree contributed by the residential coal combustion (Li et al., 2018). High levels of
343 NO_2 and SO_2 show that stringent emission mitigation strategies still need to be implemented
344 in BTH.

345 3.2.3 Sulfate, ammonium and SOA simulations in Beijing

346 The SOA and sulfate concentration directly influences the N_2O_5 heterogeneous
347 hydrolysis in the Riemer09 parameterization, and the ammonium aerosol concentration
348 substantially affects the nitrate aerosol formation. Therefore, Figure 7 presents the temporal
349 profiles of observed and calculated SOA, sulfate, and ammonium mass concentrations at
350 CRAES site in Beijing 10 to 27 February 2014. The model reasonably tracks the diurnal
351 variation of the SOA concentration compared to observations, with the MB and IOA of -1.2
352 $\mu\text{g m}^{-3}$ and 0.83, respectively. The observed SOA concentration exhibits rather large
353 fluctuations, which is not well reproduced by the model. The simulated sulfate trend is
354 generally in agreement with observations with an IOA of 0.88, but there are considerable
355 model biases. During the first pollution event, the model reasonably reproduces the sulfate
356 increase during the haze developing stage, but the early falloff of sulfate concentrations
357 during the dissipation stage causes the substantial underestimation. However, during the
358 second pollution event, the model considerably overestimates the sulfate concentration

359 against the measurement from 22 to 26 February 2014. The ammonium simulation is slightly
360 better than that of sulfate, with an IOA of 0.90.

361 Furthermore, the MFB and MFE between simulations and observations are also
362 calculated to evaluate the model performance in simulating meteorological parameters and air
363 pollutants (Table 2). Boylan and Russell (2006) have proposed that MFB should be within
364 $\pm 60\%$ and MFE should be below 75% for a satisfactory model performance. For the
365 simulation in the B-case, MFB values are within 27% and MFE values are below 55%,
366 indicating that the model performance is satisfactory.

367 In summary, the WRF-Chem model performs reasonably well in simulating air pollutants
368 and aerosol species, showing that the simulated meteorological fields and emissions used in
369 the study are generally reasonable.

370 **3.3 Contributions of the N₂O₅ heterogeneous hydrolysis and organic coating to the** 371 **nitrate formation**

372 Figure 8 provides the nitrate temporal variations in the three cases against observations
373 at CRAES site in Beijing from 10 to 27 February 2014. When the N₂O₅ heterogeneous
374 hydrolysis is not considered in the H0-case, although the model well tracks the observed
375 nitrate variations with an IOA of 0.91, it considerably underestimates nitrate concentration
376 against the measurement, with a MB of $-17.0 \mu\text{g m}^{-3}$. When the N₂O₅ heterogeneous
377 hydrolysis is taken into consideration based on the Riemer09 parameterization without
378 organic coating in the C0-case, the nitrate simulation is improved compared to that in the
379 H0-case, with an IOA of 0.95. However, the model commences to overestimate the nitrate
380 concentration compared to the measurement, with a MB of $5.4 \mu\text{g m}^{-3}$. In the B-case, when
381 all the SOA is assumed to be involved in coating to suppress the N₂O₅ heterogeneous uptake
382 on surfaces of deliquescent aerosols, the model performs best in simulating the nitrate
383 variation compared to the measurement, with the MB and IOA of $0.1 \mu\text{g m}^{-3}$ and 0.96,

384 respectively. The remarkable consistency of the simulated nitrate in the B-case with the
385 measurement indicates that the organic coating plays an important role in improving the
386 nitrate simulation. It is worth noting that the MB for nitrate aerosols at CRAES site in the
387 B-case is close to zero, but the RMSE is still rather large, reaching $19.0 \mu\text{g m}^{-3}$, showing
388 considerable underestimation and overestimation, caused by uncertainties of meteorological
389 fields and emissions. For example, the model overestimates nitrate concentrations on 11, 13,
390 and 14 February and underestimation on 24 February against measurements. In addition, the
391 early occurrence of intensified winds in the morning on 16 February in simulations cause
392 rapid falloff of nitrate concentrations, leading to substantial model biases.

393 Figure 9a presents the distribution of contributions of the N_2O_5 heterogeneous
394 hydrolysis to the nitrate formation averaged during the episode by differentiating simulations
395 in the B-case and H0-case. The contribution of the N_2O_5 heterogeneous hydrolysis to the
396 nitrate formation is substantial in BTH, exceeding $15 \mu\text{g m}^{-3}$ in the plain area. Although the
397 O_3 concentration is fairly low in BTH during the episode (Figure 6b), particularly during
398 nighttime (Figure 5b), the elevated NO_2 level still facilitates the N_2O_5 formation to warrant
399 occurrence of the N_2O_5 heterogeneous hydrolysis. Previous studies have revealed that N_2O_5
400 heterogeneous hydrolysis is vital in nitrate formation. For example, Wang et al. (2017) have
401 calculated the daily average nitrate formation potential from the N_2O_5 heterogeneous
402 hydrolysis in Beijing, showing that the reaction accounts for 52% of the total nitrate
403 formation. Su et al. (2017) have investigated the contribution of N_2O_5 heterogeneous
404 hydrolysis to the nitrate formation in Beijing during autumn in 2015 and found that the
405 reaction causes a 21.0% enhancement of nitrate concentrations. In the present study, the
406 nitrate contribution of the N_2O_5 heterogeneous hydrolysis is 29.4% in Beijing during the
407 episode on average, which is close to the result in Su et al. (2017) but much lower than that in
408 Wang et al. (2017). The average nitrate contribution of the reaction in BTH is about 30.1%,

409 showing that the reaction constitutes an important nitrate source during the haze pollution
410 episode. Additionally, the N_2O_5 heterogeneous hydrolysis contributes 11.6% of the $\text{PM}_{2.5}$
411 concentration on average, playing a considerable role in the haze formation in BTH.

412 However, it is worth noting that the brute force method (BFM) is used to quantify the
413 contribution of the N_2O_5 heterogeneous hydrolysis to the nitrate formation (Dunker et al.,
414 1996). The BFM is generally used to assess the importance of some source, but it lacks
415 consideration of interactions of the complicated physical and chemical processes in the
416 atmosphere (Zhang and Ying, 2011). Therefore, in the study, the contribution of the N_2O_5
417 heterogeneous hydrolysis to the nitrate formation might be underestimated, considering the
418 competition of inorganic cations from HNO_3 formed through gas-phase reactions and sulfate
419 aerosols in the atmosphere. It is imperative to use the source-oriented base module to
420 evaluate the nitrate contribution of the reaction.

421 Figure 9b shows the distribution of the average decrease of nitrate concentrations due to
422 suppression of organic coating during the episode by differentiating simulations in the B-case
423 and C0-case. The organic coating reduces the nitrate concentration by more than $5 \mu\text{g m}^{-3}$ in
424 the plain area of BTH, and on average, the decrease of nitrate aerosols is $4.7 \mu\text{g m}^{-3}$ or 8.4%
425 in BTH during the episode. Riemer et al. (2009) have shown that when the nitrate levels are
426 high (above $15 \mu\text{g m}^{-3}$), the organic coating decreases nitrate concentrations by 10-15% over
427 Europe. However, Cheng et al. (2018) have demonstrated that the suppression of organic
428 coating is negligible over western and central Europe, with an influence on nitrate
429 concentrations of less than 2% on average and 20% at the most significant moment.
430 Apparently, except N_2O_5 and water soluble OA in the atmosphere, the effect of organic
431 coating is also dependent on NH_3 , RH, and temperature. Hence, the inconsistency between
432 the model results about the organic coating effect can be attributed to the variation in
433 simulation conditions. For example, in order to obtain substantial effects of the organic

434 coating, N_2O_5 , SOA, and NH_3 need to be present when RH is high and temperature is low.
435 However, those conditions are rarely fulfilled simultaneously over western and central
436 Europe, causing a negligible effect of organic coating (Chen et al., 2018). Additionally, Wang
437 et al. (2017) have indicated that the evaluated nitrate level with the N_2O_5 heterogeneous
438 hydrolysis in Beijing is much higher than the observation, which they have attributed to
439 atmospheric dilution and deposition. It is worth noting that the organic coating effect might
440 constitute one of the most possible reasons for the overestimation of nitrate concentrations,
441 considering the elevated SOA level in Beijing which suppresses the N_2O_5 heterogeneous
442 hydrolysis and results in high observed N_2O_5 concentrations (Wu et al., 2017). Figure 10
443 presents the temporal variation of the simulated $\gamma_{\text{N}_2\text{O}_5}$ in Beijing during the episode. The
444 simulated $\gamma_{\text{N}_2\text{O}_5}$ fluctuates between 0.009 and 0.02 when organic coating is included, with
445 an average of 0.013. The estimated $\gamma_{\text{N}_2\text{O}_5}$ in Beijing by Wang et al. (2017) ranges from
446 0.025 to 0.072 without consideration of the suppression of organic coating, indicating that
447 organic coating substantially hinders the N_2O_5 heterogeneous hydrolysis, likely causing the
448 observed high level of N_2O_5 during nighttime.

449 It is worth noting that, in the study, the assumption of metastable aerosols is used or the
450 water soluble aerosol is assumed to be only in liquid state in simulations. However, Wang et
451 al. (2008) have highlighted the effect of the hysteresis of particle phase transitions on the
452 distribution of solid and aqueous aerosols. The aerosol phase is generally regulated by the
453 hysteresis loop. Atmospheric particles containing inorganic salts remain solid until the RH
454 reaches the DRH (deliquescence relative humidity). At the DRH, the solid particle
455 spontaneously absorbs water to become a saturated aqueous solution. However, the liquid
456 particle does not crystallize when the RH is below the DRH (Seinfeld and Pandis, 2006).
457 Therefore, another possible pathway exists to suppress the N_2O_5 hydrolysis, i.e., the inorganic
458 particles might be in solid phase without organic coating. Further studies need to be

459 conducted to evaluate the hysteresis effect on the N_2O_5 hydrolysis and organic coating.

460 **3.4 Sensitivity studies of organic aerosol hygroscopicity to the nitrate formation**

461 In section 3.3, the WRF-Chem model considerably improves nitrate simulations when
462 considering the N_2O_5 heterogeneous hydrolysis and organic coating effects. Organic aerosols
463 (OA) are broadly classified as primary OA (POA) directly emitted and SOA formed in the
464 atmosphere, some of which are water soluble. In order to explore the effects of different OA
465 coating on the nitrate formation, additional four sensitivity studies are conducted, in which
466 half of SOA (C1-case), all SOA (C2-case), all SOA and half of POA (C3-case), and all SOA
467 and POA (C4-case) are involved in coating, respectively.

468 Figure 11 shows the Taylor diagram (Taylor, 2001) to present the variance, bias and
469 correlation of the observed and simulated nitrate concentrations in the four sensitivity cases at
470 CRAES site during the episode. In the C1-case, when half of SOA is considered to involve in
471 coating, the simulated nitrate concentration is the best consistent with the observation, with a
472 correlation coefficient of 0.96. In the C2-case with all SOA assumed to engage in coating, the
473 correlation coefficient decreases to be 0.95. The normalized standardized deviation (NSD) is
474 1.02 for the C1-case and C2-case, showing the model overestimation in these two cases. With
475 half of POA involved in coating, the NSD is very close to 1.0 (0.99), indicating the simulated
476 nitrate concentration in the C3-case is almost the same as the observation on average, but the
477 correlation coefficient of 0.94 is less than those in the C1-case and C2-case. When all of OA
478 is assumed as the coating, the bias between simulated and observed nitrate concentrations is
479 the largest, and the effect of POA on suppressing the N_2O_5 heterogeneous hydrolysis might be
480 overestimated in the C4-case.

481 Sensitivity results show that the effects of different organic compounds on suppressing
482 the N_2O_5 heterogeneous hydrolysis to form nitrate varies, depending on the content of water
483 soluble OA. Laboratory and field measurements have revealed that OA becomes

484 progressively oxidized and more hygroscopic during the aging process in the atmosphere
485 (Jimenez et al., 2009). The OA hygroscopicity constitutes a necessary prerequisite for
486 accurately representing the organic coating effect on the N_2O_5 heterogeneous hydrolysis.
487 According to the simulations in the present study, in BTH, not all of SOA can serve as the
488 coating to suppress the nitrate formation, and the effect of POA on coating might be
489 neglected. Xing et al. (2019) have shown that in BTH, the heterogeneous SOA formed by
490 irreversible uptake of glyoxal and methylglyoxal on wet aerosol surfaces contributes about 30%
491 of the SOA mass during haze days. Considering the possible heterogeneous SOA contribution
492 of other carbonyl compounds and the atmospheric aging of OA, about half of SOA should
493 likely be hygroscopic and involved in coating.

494

495 **4 Conclusion**

496 Nitrate aerosol has constituted a main component of $PM_{2.5}$ with implementation of
497 aggressive emission control strategies since 2013 in BTH. In the study, the Riemer09
498 parameterization is implemented into the WRF-Chem model to simulate the nitrate formation
499 from the N_2O_5 heterogeneous hydrolysis referred to as the most important pathway of the
500 nitrate formation at nighttime. A heavy haze episode from 10 to 27 February 2014 in BTH is
501 simulated using the WRF-Chem model to verify the effect of organic coating on the N_2O_5
502 heterogeneous hydrolysis and its consequent contribution to the nitrate formation. Analyses
503 of synoptic fields show a stagnant weather condition with the prevailing southerly wind in the
504 low-level atmosphere in BTH and surrounding areas during the episode, facilitating
505 accumulation of air pollutants and heavy haze formation.

506 The WRF-Chem model performs reasonably in predicting the temporal variations of the
507 meteorological parameters compared to observations in Beijing. The model generally
508 reproduces well the temporal variations and spatial distributions of air pollutants against

509 observations at monitoring sites in BTH. In addition, the simulated diurnal profiles of sulfate,
510 ammonium and SOA are also in good agreements with the measurements at CRAES site in
511 Beijing.

512 The Riemer09 parameterization with all the SOA assumed to be involved in coating
513 considerably improves the nitrate simulations compared to the measurements at CRAES site
514 in Beijing. When organic coating is not considered in the Riemer09 parameterization, the
515 model overestimates the nitrate concentration against the measurements. On average, organic
516 coating decreases nitrate concentrations by $4.7 \mu\text{g m}^{-3}$ or 8.4% in BTH during the episode.
517 Furthermore, the N_2O_5 heterogeneous hydrolysis with organic coating contributes about 30.1%
518 of nitrate concentrations, and 11.6% of the $\text{PM}_{2.5}$ concentration in BTH, playing a
519 considerable role in the haze formation.

520 Sensitivity studies reveal that the OA hygroscopicity is a necessary prerequisite for
521 accurately evaluating the organic coating effect on the N_2O_5 heterogeneous hydrolysis. In the
522 present study, POA might not serve as coating and about half of SOA should be involved in
523 coating to suppress the nitrate formation. Future studies still need to be conducted to further
524 predict the OA hygroscopicity, in order to more precisely represent the organic coating effect
525 on the N_2O_5 heterogeneous hydrolysis in chemical transport models.

526

527

528 *Author contribution.* Guohui Li, as the contact author, provided the ideas and financial
529 support, verified the conclusions, and revised the paper. Lang Liu conducted a research,
530 designed the experiments, carried the methodology out, performed the simulation, processed
531 the data, prepared the data visualization, and prepared the manuscript with contributions from
532 all authors. Jiarui Wu and Xia Li provided the treatment of meteorological data, analyzed the
533 study data, validated the model performance, and reviewed the manuscript. Suixin Liu, Yang

534 Qian, Tian Feng, and Jiamao Zhou provided the observation data used in the study,
535 synthesized the observation, and reviewed the paper. Xuexi Tie and Junji Cao provided
536 critical reviews pre-publication stage.

537

538

539 *Acknowledgements.* This work is financially supported by the National Key R&D Plan
540 (Quantitative Relationship and Regulation Principle between Regional Oxidation Capacity of
541 Atmospheric and Air Quality (2017YFC0210000)) and National Research Program for Key
542 Issues in Air Pollution Control.

543

544

545

546

547

548 **References**

- 549 Aiken, A. C., DeCarlo, P. F., Kroll, J. H., Worsnop, D. R., Huffman, J. A., Docherty, K. S.,
550 Ulbrich, I. M., Mohr, C., Kimmel, J. R., Sueper, D., Sun, Y., Zhang, Q., Trimborn, A.,
551 Northway, M., Ziemann, P. J., Canagaratna, M. R., Onasch, T. B., Alfarra, M. R., Prévôt,
552 A. S. H., Dommen, J., Duplissy, J., Metzger, A., Baltensperger, U., and Jimenez, J. L.: O
553 / C and OM / OC Ratios of Primary, Secondary, and Ambient Organic Aerosols with
554 High-Resolution Time-of-Flight Aerosol Mass Spectrometry, *Environ. Sci. Technol.*, 42,
555 4478–4485, <https://doi.org/10.1021/es703009q>, 2008.
- 556 Anttila, T., Kiendlerscharr, A., Tillmann, R., and Mentel, T. F.: On the reactive uptake of
557 gaseous compounds by organic-coated aqueous aerosols: theoretical analysis and
558 application to the heterogeneous hydrolysis of N₂O₅, *J. Phys. Chem. A*, 110, 10435–
559 10443, <https://doi.org/10.1021/jp062403c>, 2006.
- 560 Bei, N., Wu, J., Elser, M., Feng, T., Cao, J., El-Haddad, I., Li, X., Huang, R., Li, Z., Long, X.,
561 Xing, L., Zhao, S., Tie, X., Prévôt, A. S. H., and Li, G.: Impacts of meteorological
562 uncertainties on the haze formation in Beijing–Tianjin–Hebei (BTH) during wintertime:
563 a case study, *Atmos. Chem. Phys.*, 17, 14579–14591,
564 <https://doi.org/10.5194/acp-17-14579-2017>, 2017.
- 565 Bertram, T. H. and Thornton, J. A.: Toward a general parameterization of N₂O₅ reactivity on
566 aqueous particles: the competing effects of particle liquid water, nitrate and chloride,
567 *Atmos. Chem. and Phys.*, 9, 8351–8363, <https://doi.org/10.5194/acp-9-8351-2009>, 2009.
- 568 Binkowski, F. S. and Roselle, S. J.: Models-3 Community Multiscale Air Quality (CMAQ)
569 model aerosol component 1. Model description, *J. Geophys. Res.-Atmos.*, 108, 335–346,
570 <https://doi.org/10.1029/2001JD001409>, 2003.
- 571 Boylan, J. W. and Russell, A. G.: PM and light extinction model performance metrics, goals,
572 and criteria for three-dimensional air quality models, *Atmos. Environ.*, 40, 4946–4959,
573 <https://doi.org/10.1016/j.atmosenv.2005.09.087>, 2006.
- 574 Brown, S. S., Dubé, W. P., Tham, Y. J., Zha, Q., Xue, L., Poon, S., Wang, Z., Blake, D. R.,
575 Tsui, W., Parrish, D. D., and Wang, T.: Nighttime chemistry at a high altitude site above
576 Hong Kong, *J. Geophys. Res.-Atmos.*, 121, 2457–2475,
577 <https://doi.org/10.1002/2015JD024566>, 2016.
- 578 Brown, S. S., Ryerson, T. B., Wollny, A. G., Brock, C. A., Peltier, R., Sullivan, A. P., Weber,
579 R. J., Dubé, W. P., Trainer, M., and Meagher, J. F.: Variability in Nocturnal Nitrogen
580 Oxide Processing and Its Role in Regional Air Quality, *Science*, 311, 67–70,
581 <https://doi.org/10.1126/science.1120120>, 2006.
- 582 Cao, J. J., Lee, S. C., Ho, K. F., Zou, S. C., Fung, K., Li, Y., Watson, J. G., and Chow, J. C.:
583 Spatial and seasonal variations of atmospheric organic carbon and elemental carbon in
584 Pearl River Delta Region, China, *Atmos. Environ.*, 38, 4447–4456,
585 <https://doi.org/10.1016/j.atmosenv.2004.05.016>, 2004.
- 586 Cao, J. J., Lee, S. C., Chow, J. C., Watson, J. G., Ho, K. F., Zhang, R. J., Jin, Z. D., Shen, Z.
587 X., Chen, G. C., Kang, Y. M., Zou, S. C., Zhang, L. Z., Qi, S. H., Dai, M. H., Cheng, Y.,
588 and Hu, K.: Spatial and seasonal distributions of carbonaceous aerosols over China, *J.*
589 *Geophys. Res.-Atmos.*, 112, D22S11, <https://doi.org/10.1029/2006JD008205>, 2007.
- 590 Chang, W. L., Bhave, P. V., Brown, S. S., Riemer, N., Stutz, J., and Dabdub, D.:
591 Heterogeneous Atmospheric Chemistry, Ambient Measurements, and Model

592 Calculations of N₂O₅: A Review, *Aerosol Sci. and Tech.*, 45, 665–695,
593 <https://doi.org/10.1080/02786826.2010.551672>, 2011.

594 Chen, F. and Dudhia, J.: Coupling an advanced land surface-hydrology model with the Penn
595 State-NCAR MM5 modeling system. Part I: Model implementation and sensitivity, *Mon.*
596 *Weather Rev.*, 129, 569–585,
597 [https://doi.org/10.1175/1520-0493\(2001\)129<0569:CAALSH>2.0.CO;2](https://doi.org/10.1175/1520-0493(2001)129<0569:CAALSH>2.0.CO;2), 2001.

598 Chen, Y., Wolke, R., Ran, L., Birmili, W., Spindler, G., Schroder, W., Su, H., Cheng, Y.,
599 Tegen, I., and Wiedensoher, A.: A Parameterization of Heterogeneous Hydrolysis of
600 N₂O₅ for mass-based aerosol models: Improvement of Particulate Nitrate Prediction,
601 *Atmos. Chem. and Phys.*, 8, 673–689, <https://doi.org/10.5194/acp-18-673-2018>, 2018.

602 Chou, M. D. and Suarez, M. J.: A solar radiation parameterization for atmospheric studies,
603 NASA TM-104606, Nasa Tech. memo 15, 1999.

604 Chou, M. D., Suarez, M. J., Liang, X. Z., Yan, M. H., and Cote, C.: A Thermal Infrared
605 Radiation Parameterization for Atmospheric Studies, NASA TM-2001-104606, Max J.,
606 19, 2001.

607 Davis, J. M., Bhave, P. V., and Foley, K. M.: Parameterization of N₂O₅ reaction probabilities
608 on the surface of particles containing ammonium, sulfate, and nitrate, *Atmos. Chem. and*
609 *Phys.*, 8, 5295–5311, <https://doi.org/10.5194/acp-8-5295-2008>, 2008.

610 Dentener, F. J. and Crutzen, P. J.: Reaction of N₂O₅ on tropospheric aerosols: Impact on the
611 global distributions of NO_x, O₃, and OH, *J. Geophys. Res.-Atmos.*, 98, 7149–7163,
612 <https://doi.org/10.1029/92JD02979>, 1993.

613 Dunker, A. M., Morris, R. E., Pollack, A. K., Schleyer, C. H., and Yarwood, G:
614 Photochemical modeling of the impact of fuels and vehicles on urban ozone using auto
615 oil program data, *Environ. Sci. Technol.*, 30, 787–801,
616 <https://doi.org/10.1021/es950175m>, 1996.

617 Evans, M. J. and Jacob, D. J.: Impact of new laboratory studies of N₂O₅ hydrolysis on global
618 model budgets of tropospheric nitrogen oxides, ozone, and OH, *Geophys. Res. Lett.*, 32,
619 297–314, <https://doi.org/10.1029/2005GL022469>, 2005.

620 Feng, T., Li, G., Cao, J., Bei, N., Shen, Z., Zhou, W., Liu, S., Zhang, T., Wang, Y., Huang,
621 R.-J., Tie, X., and Molina, L. T.: Simulations of organic aerosol concentrations during
622 springtime in the Guanzhong Basin, China, *Atmos. Chem. Phys.*, 16, 10045–10061,
623 <https://doi.org/10.5194/acp-16-10045-2016>, 2016.

624 Fountoukis, C., Nenes, A., Sullivan, A., Weber, R., VanReken, T., Fischer, M., Matias, E.,
625 Moya, M. Farmer, D., and Cohen, R.: Thermodynamic characterization of Mexico City
626 Aerosol during MILAGRO 2006, *Atmos. Chem. Phys.*, 9, 2141–2156, 2009.

627 Gao, M., Carmichael, G. R., Wang, Y., Saide, P. E., Yu, M., Xin, J., Liu, Z., and Wang, Z.:
628 Modeling study of the 2010 regional haze event in the North China Plain, *Atmos. Chem.*
629 *Phys.*, 16, 1673–1691, <https://doi.org/10.5194/acp-16-1673-2016>, 2016.

630 Grell, G. A., Peckham, S. E., Schmitz, R., McKeen, S. A., Frost, G., Skamarock, W. C., and
631 Eder, B.: Fully coupled “online” chemistry within the WRF model, *Atmos. Environ.*, 39,
632 6957–6975, 2005.

633 Guenther, A., Karl, T., Harley, P., Wiedinmyer, C., Palmer, P. I., and Geron, C.: Estimates of
634 global terrestrial isoprene emissions using MEGAN (Model of Emissions of Gases and

635 Aerosols from Nature), *Atmos. Chem. and Phys.*, 6, 3181–3210,
636 <https://doi.org/10.5194/acp-6-3181-2006>, 2006.

637 Guo, S., Hu, M., Zamora, M. L., Peng, J., Shang, D., Zheng, J., Du, Z., Wu, Z., Shao, M., and
638 Zeng, L.: Elucidating severe urban haze formation in China, *P. Natl. Acad. Sci. USA*,
639 111, 17373–17378, <https://doi.org/10.1073/pnas.1419604111>, 2014.

640 Hess, P. G., Flocke, S., Lamarque, J. F., Barth, M. C., and Madronich, S.: Episodic modeling
641 of the chemical structure of the troposphere as revealed during the spring MLOPEX 2
642 intensive, *J. Geophys. Res.-Atmos.*, 105, 26, 809–839, 2000.

643 Hong, S. Y. and Lim, J. O. J.: The WRF Single-Moment 6-Class Microphysics Scheme
644 (WSM6), *Asia-Pacif. J. Atmos. Sci.*, 42, 129–151, 2006.

645 Horowitz, L. W., Walters, S., Mauzerall, D. L., Emmons, L. K., Rasch, P. J., Granier, C., Tie,
646 X., Lamarque, J. F., Schultz, M. G., Tyndall, G. S., Orlando, J. J., and Brasseur, G. P.: A
647 global simulation of tropospheric ozone and related tracers: Description and evaluation
648 of MOZART, version 2, *J. Geophys. Res.-Atmos.*, 108, 4784,
649 <https://doi.org/10.1029/2002JD002853>, 2003.

650 Janjić, Z. I.: Nonsingular Implementation of the Mellor-Yamada Level 2.5 Scheme in the
651 NCEP Meso Model, NCEP Office Note 437, 2002.

652 Jimenez, J. L., Canagaratna, M. R., Donahue, N. M., Prevot, A. S. H., Zhang, Q., Kroll, J. H.,
653 DeCarlo, P. F., Allan, J. D., Coe, H., Ng, N. L., Aiken, A. C., Docherty, K. S., Ulbrich, I.
654 M., Grieshop, A. P., Robinson, A. L., Duplissy, J., Smith, J. D., Wilson, K. R., Lanz, V.
655 A., Hueglin, C., Sun, Y. L., Tian, J., Laaksonen, A., Raatikainen, T., Rautiainen, J.,
656 Vaattovaara, P., Ehn, M., Kulmala, M., Tomlinson, J. M., Collins, D. R., Cubison, M. J.,
657 Dunlea, E. J., Huffman, J. A., Onasch, T. B., Alfarra, M. R., Williams, P. I., Bower, K.,
658 Kondo, Y., Schneider, J., Drewnick, F., Borrmann, S., Weimer, S., Demerjian, K.,
659 Salcedo, D., Cottrell, L., Griffin, R., Takami, A., Miyoshi, T., Hatakeyama, S., Shimono,
660 A., Sun, J. Y., Zhang, M. Y., Dzepina, K., Kimmel, J. R., Sueper, D., Jayne, J. T.,
661 Herndon, S. C., Trimborn, A. M., Williams, L. R., Wood, E. C., Middlebrook, A. M.,
662 Kolb, C. E., Baltensperger, U., and Worsnop, D. R.: Evolution of organic aerosols in the
663 atmosphere, *Science*, 326(5959), 1525–1529, <https://doi.org/10.1126/science.1180353>,
664 2009.

665 Kim, Y. J., Spak, S. N., Carmichael, G. R., Riemer, N., and Stanier, C. O.: Modeled aerosol
666 nitrate formation pathways during wintertime in the Great Lakes region of North
667 America, *J. Geophys. Res.-Atmos.*, 119, 12420–12445,
668 <https://doi.org/10.1002/2014JD022320>, 2014.

669 Li, G., Bei, N., Cao, J., Huang, R., Wu, J., Feng, T., Wang, Y., Liu, S., Zhang, Q., Tie, X.,
670 and Molina, L. T.: A possible pathway for rapid growth of sulfate during haze days in
671 China, *Atmos. Chem. Phys.*, 17, 3301–3316, <https://doi.org/10.5194/acp-17-3301-2017>,
672 2017.

673 Li, G., Bei, N., Tie, X., and Molina, L. T.: Aerosol effects on the photochemistry in Mexico
674 City during MCMA-2006/MILAGRO campaign, *Atmos. Chem. and Phys.*, 11, 5169–
675 5182, <https://doi.org/10.5194/acp-11-5169-2011>, 2011a.

676 Li, G., Lei, W., Bei, N., and Molina, L. T.: Contribution of garbage burning to chloride and
677 PM_{2.5} in Mexico City, *Atmos. Chem. and Phys.* 12, 8751–8761,
678 <https://doi.org/10.5194/acp-12-8751-2012>, 2012.

- 679 Li, G., Lei, W., Zavala, M., Volkamer, R., Dusanter, S., Stevens, P., and Molina, L. T.:
680 Impacts of HONO sources on the photochemistry in Mexico City during the
681 MCMA-2006/MILAGO Campaign, *Atmos. Chem. and Phys.*, 10, 6551–6567,
682 <https://doi.org/10.5194/acp-10-6551-2010>, 2010.
- 683 Li, G., Zavala, M., Lei, W., Tsimpidi, A. P., Karydis, V. A., Pandis, S. N., Canagaratna, M.
684 R., and Molina, L. T.: Simulations of organic aerosol concentrations in Mexico City
685 using the WRF-Chem model during the MCMA-2006/MILAGRO campaign, *Atmos.*
686 *Chem. and Phys.*, 11, 3789–3809, <https://doi.org/10.5194/acp-11-3789-2011>, 2011b.
- 687 Li, G., Zhang, R., Fan, J., and Tie, X.: Impacts of black carbon aerosol on photolysis and
688 ozone, *J. Geophys. Res.-Atmos.*, 110, D23206, <https://doi.org/10.1029/2005JD005898>,
689 2005.
- 690 Li, X., Wu, J., Elser, M., Feng, T., Cao, J., El-Haddad, I., Huang, R., Tie, X., Prévôt, A. S. H.,
691 and Li, G.: Contributions of residential coal combustion to the air quality in Beijing–
692 Tianjin–Hebei (BTH), China: a case study, *Atmos. Chem. Phys.*, 18, 10675–10691,
693 <https://doi.org/10.5194/acp-18-10675-2018>, 2018.
- 694 Liggió, J., Li, S. M., and McLaren, R.: Reactive uptake of glyoxal by particulate matter, *J.*
695 *Geophys. Res.-Atmos.*, 110, doi: 10.1029/2004jd005113, 2005.
- 696 Liu, W., Shen, G., Chen, Y., Shen, H., Huang, Y., Li, T., Wang, Y., Fu, X., Tao, S., Liu, W.,
697 Huang-Fu, Y., Zhang, W., Xue, C., Liu, G., Wu, F. and Wong, M.: Air pollution and
698 inhalation exposure to particulate matter of different sizes in rural households using
699 improved stoves in central China, *J. Environ. Sci.-China*, 63, 87–95,
700 doi:10.1016/j.jes.2017.06.019, 2018.
- 701 Lowe, D., Archer-Nicholls, S., Morgan, W., Allan, J., Utembe, S., Ouyang, B., Aruffo, E., Le
702 Breton, M., Zaveri, R. A., Di Carlo, P., Percival, C., Coe, H., Jones, R., and McFiggans,
703 G.: WRF-Chem model predictions of the regional impacts of N₂O₅ heterogeneous
704 processes on night-time chemistry over north-western Europe, *Atmos. Chem. Phys.*, 15,
705 1385–1409, <https://doi.org/10.5194/acp-15-1385-2015>, 2015.
- 706 Nenes, A., Pandis, S. N., and Pilinis, C.: ISORROPIA: A new thermodynamic equilibrium
707 model for multiphase multicomponent inorganic aerosols, *Aquat. Geochem.*, 4, 123–152,
708 <https://doi.org/10.1023/a:1009604003981>, 1998.
- 709 Riemer, N., Vogel, H., Vogel, B., Schell, B., Ackermann, I., Kessler, C., and Hass, H.:
710 Impact of the heterogeneous hydrolysis of N₂O₅ on chemistry and nitrate aerosol
711 formation in the lower troposphere under photochemical conditions, *J. Geophys.*
712 *Res.-Atmos.*, D4, 4144, <https://doi.org/10.1029/2002JD002436>, 2003.
- 713 Riemer, N., Vogel, H., Vogel, B., Anttila, T., Kiendler-Scharr, A., and Mentel, T.F.: Relative
714 importance of organic coatings for the heterogeneous hydrolysis of N₂O₅ during summer
715 in Europe, *J. Geophys. Res.-Atmos.*, D17307, <https://doi.org/10.1029/2008JD011369>,
716 2009.
- 717 Robinson, A. L., Donahue, N. M., Shrivastava, M. K., Weitkamp, E. A., Sage, A. M.,
718 Grieshop, A. P., Lane, T. E., Pandis, S. N., and Pierce, J. R.: Rethinking organic aerosols:
719 semivolatile emissions and photochemical aging, *Science*, 315, 1259–1262, 2007.
- 720 Seinfeld, J. H. and Pandis, S. N.: *Atmospheric Chemistry and Physics: From Air Pollution to*
721 *Climate Change*, 2nd Edn., John Wiley & Sons Inc., New York, 2006.

- 722 Shrivastava, M. K., Lane, T. E., Donahue, N. M., Pandis, S. N., and Robinson, A. L.: Effects
723 of gas particle partitioning and aging of primary emissions on urban and regional
724 organic aerosol concentrations, *J. Geophys. Res.-Atmos.*, 113, doi:
725 10.1029/2007jd009735, 2008.
- 726 Strader, R.: Evaluation of secondary organic aerosol formation in winter, *Atmos. Environ.*, 33,
727 4849–4863, [https://doi.org/10.1016/s1352-2310\(99\)00310-6](https://doi.org/10.1016/s1352-2310(99)00310-6), 1999.
- 728 Sun, Y. L., Wang, Z. F., Fu, P. Q., Yang, T., Jiang, Q., Dong, H. B., Li, J., and Jia, J. J.:
729 Aerosol composition, sources and processes during wintertime in Beijing, China, *Atmos.*
730 *Chem. Phys.*, 13, 4577–4592, <https://doi.org/10.5194/acp-13-4577-2013>, 2013.
- 731 Sun, Y. L., Wang, Z. F., Du, W., Zhang, Q., Wang, Q. Q., Fu, P. Q., Pan, X. L., Li, J., Jayne,
732 J., and Worsnop, D. R.: Long-term real-time measurements of aerosol particle
733 composition in Beijing, China: seasonal variations, meteorological effects, and source
734 analysis, *Atmos. Chem. Phys.*, 15, 10149–10165,
735 <https://doi.org/10.5194/acp-15-10149-2015>, 2015.
- 736 Tao, J., Zhang, L., Cao, J., and Zhang, R.: A review of current knowledge concerning
737 PM_{2.5} chemical composition, aerosol optical properties and their relationships across
738 China, *Atmos. Chem. Phys.*, 17, 9485–9518, <https://doi.org/10.5194/acp-17-9485-2017>,
739 2017.
- 740 Taylor, K. E.: Summarizing multiple aspects of model performance in a single diagram, *J.*
741 *Geophys. Res.-Atmos.*, 106(D7), 7183–7192, <https://doi.org/10.1029/2000JD900719>,
742 2001.
- 743 Tie, X., Madronich, S., Walters, S., Zhang, R., Rasch, P., and Collins, W.: Effect of clouds on
744 photolysis and oxidants in the troposphere, *J. Geophys. Res.-Atmos.*, 108, 4642,
745 <https://doi.org/10.1029/2003JD003659>, 2003.
- 746 Volkamer, R., Martini, F. S., Molina, L. T., Salcedo, D., Jimenez, J. L., and Molina, M. J.: A
747 missing sink for gas-phase glyoxal in Mexico City: Formation of secondary organic
748 aerosol, *Geophys. Res. Lett.*, 34, doi: 10.1029/2007gl030752, 2007.
- 749 Wang, G., Zhang, R., Gomez, M. E., Yang, L., Levy Zamora, M., Hu, M., Lin, Y., Peng, J.,
750 Guo, S., Meng, J., Li, J., Cheng, C., Hu, T., Ren, Y., Wang, Y., Gao, J., Cao, J., An, Z.,
751 Zhou, W., Li, G., Wang, J., Tian, P., Marrero-Ortiz, W., Secrest, J., Du, Z., Zheng, J.,
752 Shang, D., Zeng, L., Shao, M., Wang, W., Huang, Y., Wang, Y., Zhu, Y., Li, Y., Hu, J.,
753 Pan, B., Cai, L., Cheng, Y., Ji, Y., Zhang, F., Rosenfeld, D., Liss, P. S., Duce, R. A.,
754 Kolb, C. E., and Molina, M. J.: Persistent sulfate formation from London Fog to Chinese
755 haze, *P. Natl. Acad. Sci. USA*, 113(48), 13630–13635,
756 <https://doi.org/10.1073/pnas.1616540113>, 2016.
- 757 Wang, H., Lu, K., Chen, X., Zhu, Q., Chen, Q., Guo, S., Jiang, M., Li, X., Shang, D., Tan, Z.,
758 Wu, Y., Wu, Z., Zou, Q., Zheng, Y., Zeng, L., Zhu, T., Hu, M., and Zhang, Y.: High
759 N₂O₅ concentrations observed in urban Beijing: Implications of a large nitrate formation
760 Pathway, *Environ. Sci. Tech. Lett.*, 4, 416–420,
761 <https://doi.org/10.1021/acs.estlett.7b00341>, 2017.
- 762 Wang, J., Hoffmann, A. A., Park, R. J., Jacob, D. J., and Martin, S. T.: Global distribution of
763 solid and aqueous sulfate aerosols: Effect of the hysteresis of particle phase transitions, *J.*
764 *Geophys. Res.-Atmos.*, 113, D11206, <https://doi.org/10.1029/2007JD009367>, 2008.
- 765 Wei, S., Shen, G., Zhang, Y., Xue, M., Xie, H., Lin, P., Chen, Y., Wang, X. and Tao, S.:

766 Field measurement on the emissions of PM, OC, EC and PAHs from indoor crop straw
767 burning in rural China, *Environ. Pollut.*, 184, 18–24, doi:10.1016/j.envpol.2013.07.036,
768 2014.

769 Wesely, M. L.: Parameterization of surface resistances to gaseous dry deposition in
770 regional-scale numerical models, *Atmos. Environ.*, 23, 1293–1304,
771 [https://doi.org/10.1016/0004-6981\(89\)90153-4](https://doi.org/10.1016/0004-6981(89)90153-4), 1989.

772 Wu, J., Li, G., Cao, J., Bei, N., Wang, Y., Feng, T., Huang, R., Liu, S., Zhang, Q., and Tie, X.:
773 Contributions of trans-boundary transport to summertime air quality in Beijing, China,
774 *Atmos. Chem. Phys.*, 17, 2035–2051, <https://doi.org/10.5194/acp-17-2035-2017>, 2017.

775 Xing, L., Wu, J., Elser, M., Tong, S., Liu, S., Li, X., Liu, L., Cao, J., Zhou, J., El-Haddad, I.,
776 Huang, R., Ge, M., Tie, X., Prévôt, A. S. H., and Li, G.: Wintertime secondary organic
777 aerosol formation in Beijing–Tianjin–Hebei (BTH): contributions of HONO sources and
778 heterogeneous reactions, *Atmos. Chem. Phys.*, 19, 2343–2359,
779 <https://doi.org/10.5194/acp-19-2343-2019>, 2019.

780 Yu, X. Y., Cary, R. A., and Laulainen, N. S.: Primary and secondary organic carbon
781 downwind of Mexico City, *Atmos. Chem. Phys.*, 9, 6793–6814,
782 <https://doi.org/10.5194/acp-9-6793-2009>, 2009.

783 Zhang, H. and Ying, Q.: Secondary organic aerosol formation and source apportionment in
784 Southeast Texas, *Atmos. Environ.*, 45: 3217–3227,
785 <https://doi.org/10.1016/j.atmosenv.2011.03.046>, 2011.

786 Zhang, Q., Streets, D. G., Carmichael, G. R., He, K., Huo, H., Kannari, A., Klimont, Z., Park,
787 I. S., Reddy, S., Fu, J., Chen, D., Duan, L., Lei, Y., Wang, L., and Yao, Z.: Asian
788 emissions in 2006 for the NASA INTEX-B mission, *Atmos. Chem. and Phys.*, 9, 5131–
789 5153, <https://doi.org/10.5194/acp-9-5131-2009>, 2009.

790 Zhang, R., Jing, J., Tao, J., Hsu, S., Wang, G., Cao, J., Lee, C., Zhu, L., Chen, Z., and Zhao,
791 Y.: Chemical characterization and source apportionment of PM_{2.5} in Beijing: seasonal
792 perspective, *Atmos. Chem. and Phys.*, 13, 7053–7074,
793 <https://doi.org/10.5194/acp-13-7053-2013>, 2013.

794 Zhang, X. Y., Wang, J. Z., Wang, Y. Q., Liu, H. L., Sun, J. Y., and Zhang, Y. M.: Changes in
795 chemical components of aerosol particles in different haze regions in China from 2006
796 to 2013 and contribution of meteorological factors, *Atmos. Chem. and Phys.*, 15, 19197–
797 19238, <https://doi.org/10.5194/acp-15-12935-2015>, 2015.

798 Zhang, X. Y., Wang, Y. Q., Niu, T., Zhang, X. C., Gong, S. L., Zhang, Y. M., and Sun, J. Y.:
799 Atmospheric aerosol compositions in China: spatial/temporal variability, chemical
800 signature, regional haze distribution and comparisons with global aerosols, *Atmos.*
801 *Chem. and Phys.*, 12, 779–799, <https://doi.org/10.5194/acp-12-779-2012>, 2012.

802 Zhao, J., Levitt, N. P., Zhang, R., and Chen, J.: Heterogeneous reactions of methylglyoxal in
803 acidic media: Implications for secondary organic aerosol formation, *Environ. Sci.*
804 *Technol.*, 40, 7682–7687, doi: 10.1021/es060610k, 2006.

805 Zhao, P. S., Dong, F., He, D., Zhao, X. J., Zhang, X. L., Zhang, W. Z., Yao, Q., and Liu, H.
806 Y.: Characteristics of concentrations and chemical compositions for PM_{2.5} in the region
807 of Beijing, Tianjin, and Hebei, China, *Atmos. Chem. and Phys.*, 13, 4631–4644,
808 <https://doi.org/10.5194/acp-13-4631-2013>, 2013.

809 Zheng, B., Zhang, Q., Zhang, Y., He, K. B., Wang, K., Zheng, G. J., Duan, F. K., and Ma, Y.
810 L., Kimoto, T.: Heterogeneous chemistry: a mechanism missing in current models to
811 explain secondary inorganic aerosol formation during the January 2013 haze episode in
812 North China, *Atmos. Chem. and Phys.*, 2031–2049,
813 <https://doi.org/10.5194/acp-15-2031-2015>, 2015.

814

815

816

817

818

819 **Table 1** WRF-Chem model configurations.

820

Regions	Beijing-Tianjin-Hebei (BTH)
Simulation period	February 10 to 27, 2014
Domain size	200 × 200
Domain center	38.0°N, 116.0°E
Horizontal resolution	6km × 6km
Vertical resolution	35 vertical levels with a stretched vertical grid with spacing ranging from 30m near the surface, to 500m at 2.5km and 1km above 14km
Microphysics scheme	WSM 6-class graupel scheme (Hong and Lim, 2006)
Boundary layer scheme	MYJ TKE scheme (Janjić, 2002)
Surface layer scheme	MYJ surface scheme (Janjić, 2002)
Land-surface scheme	Unified Noah land-surface model (Chen and Dudhia, 2001)
Long-wave radiation scheme	Goddard longwave scheme (Chou and Suarez, 2001)
Short-wave radiation scheme	Goddard shortwave scheme (Chou and Suarez, 1999)
Meteorological boundary and initial conditions	NCEP 1°×1° reanalysis data
Chemical initial and boundary conditions	MOZART 6-hour output (Horowitz et al., 2003)
Anthropogenic emission inventory	SAPRC-99 chemical mechanism emissions (Zhang et al., 2009)
Biogenic emission inventory	MEGAN model developed by Guenther et al. (2006)
Model spin-up time	24 hours

821

822

823

824

825

826 Table 2 Statistics for model performance.
827

	MFB (%)	MFE (%)	MB	RMSE	IOA
^a Temperature	-3.7	8.5	-0.2 °C	1.7 °C	0.94
^a Relative humidity	5.2	15.7	2.6 %	10.9 %	0.89
^a Wind speed	16.3	38.6	0.3 m s ⁻¹	1.0 m s ⁻¹	0.73
^a Wind direction	26.3	54.6	21.9 °	90.4 °	0.66
^b PM _{2.5}	-3.0	13.5	-6.3 µg m ⁻³	27.6 µg m ⁻³	0.96
^b O ₃	2.1	28.3	1.4 µg m ⁻³	10.3 µg m ⁻³	0.91
^b NO ₂	10.6	16.2	6.6 µg m ⁻³	13.0 µg m ⁻³	0.92
^b SO ₂	6.1	23.9	7.6 µg m ⁻³	27.8 µg m ⁻³	0.85
^b CO	10.6	18.5	0.2 mg m ⁻³	0.5 mg m ⁻³	0.90
^c SOA	-14.5	52.9	-1.2 µg m ⁻³	15.5 µg m ⁻³	0.83
^c Sulfate	23.8	53.0	4.5 µg m ⁻³	26.5 µg m ⁻³	0.88
^c Ammonium	22.2	44.2	2.9 µg m ⁻³	16.4 µg m ⁻³	0.90
^c Nitrate	7.1	37.1	0.1 µg m ⁻³	19.0 µg m ⁻³	0.96

828 a, b, and c represent the meteorological parameter averaged over 12 meteorological sites in
829 Beijing, the air pollutant averaged over all ambient monitoring stations in BTH, and the
830 aerosol component at the CRAES site in Beijing, respectively.

831
832
833
834
835

Figure Captions

836

837

838 Figure 1 WRF-Chem simulation domain with topography. The red filled circles show the
839 locations of the cities with ambient air quality monitoring sites, and the size of the
840 circles represents the number of sites in each city. The blue filled rectangle denotes the
841 CRAES observation site in Beijing.

842 Figure 2 Distributions of average winds (black flag vectors), geopotential heights (blue lines),
843 temperature (red lines), and relative humidity (contour fill) at (a) and (b) 500hPa and
844 (c) and (d) 850hPa from 10 to 27 February 2014, respectively.

845 Figure 3 Temporal variations of simulated (red line) and observed (black dots) meteorological
846 parameters of near-surface (a) temperature, (b) relative humidity, (c) wind speed, and
847 (d) wind direction averaged at 12 meteorological sites in Beijing from 10 to 27
848 February 2014.

849 Figure 4 Relationships between observed and simulated mass concentrations of PM_{2.5}, O₃,
850 NO₂, SO₂, and CO in Beijing, Tianjin, and Hebei from 10 to 27 February 2014. The
851 red line is the linear regression between observations and simulations, and the black
852 dashed line presents the 1:1 line.

853 Figure 5 Comparison of observed (black dots) and simulated (red line) diurnal profiles of
854 near surface hourly (a) PM_{2.5}, (b) O₃, (c) NO₂, (d) SO₂, and (e) CO averaged over all
855 ambient monitoring stations in BTH from 10 to 27 February 2014.

856 Figure 6 Spatial distributions of average (a) PM_{2.5}, (b) O₃, (c) NO₂, and (d) SO₂ mass
857 concentrations from 10 to 27 February 2014. Colored dots, colored contour, and black
858 arrows are observations, simulations, and simulated surface winds, respectively.

859 Figure 7 Comparison of observed (black dots) and simulated (red line) diurnal profiles of
860 hourly (a) SOA, (b) sulfate, and (c) ammonium concentrations at CRAES site in
861 Beijing from 10 to 27 February 2014.

862 Figure 8 Temporal variations of observed (black dot) and the simulated (Green line: H0-case;
863 Blue line: C0-case; Red line: B-case) nitrate concentrations at CRAES site in Beijing
864 from 10 to 27 February 2014.

865 Figure 9 Spatial distributions of average nitrate contributions of (a) the N₂O₅ heterogeneous
866 hydrolysis and (b) organic coating in BTH from 10 to 27 February 2014.

867 Figure 10 Temporal variation of the simulated $\gamma_{N_2O_5}$ in the B-case in Beijing from 10 to 27
868 February 2014.

869 Figure 11 Taylor diagram (Taylor, 2001) to present the variance, bias and correlation of the
870 observed and simulated nitrate concentrations at CRAES site in Beijing from 10 to 27
871 February 2014.

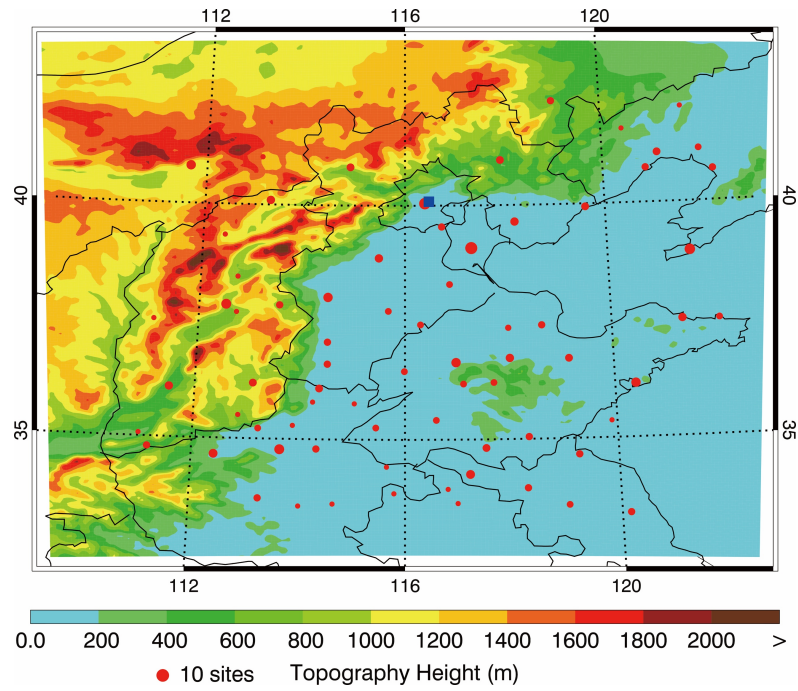
872

873

874

875

876



877

878

879 Figure 1 WRF-Chem simulation domain with topography. The red filled circles show the
 880 locations of the cities with ambient air quality monitoring sites, and the size of the circles
 881 represents the number of sites in each city. The blue filled rectangle denotes the CRAES
 882 observation site in Beijing.

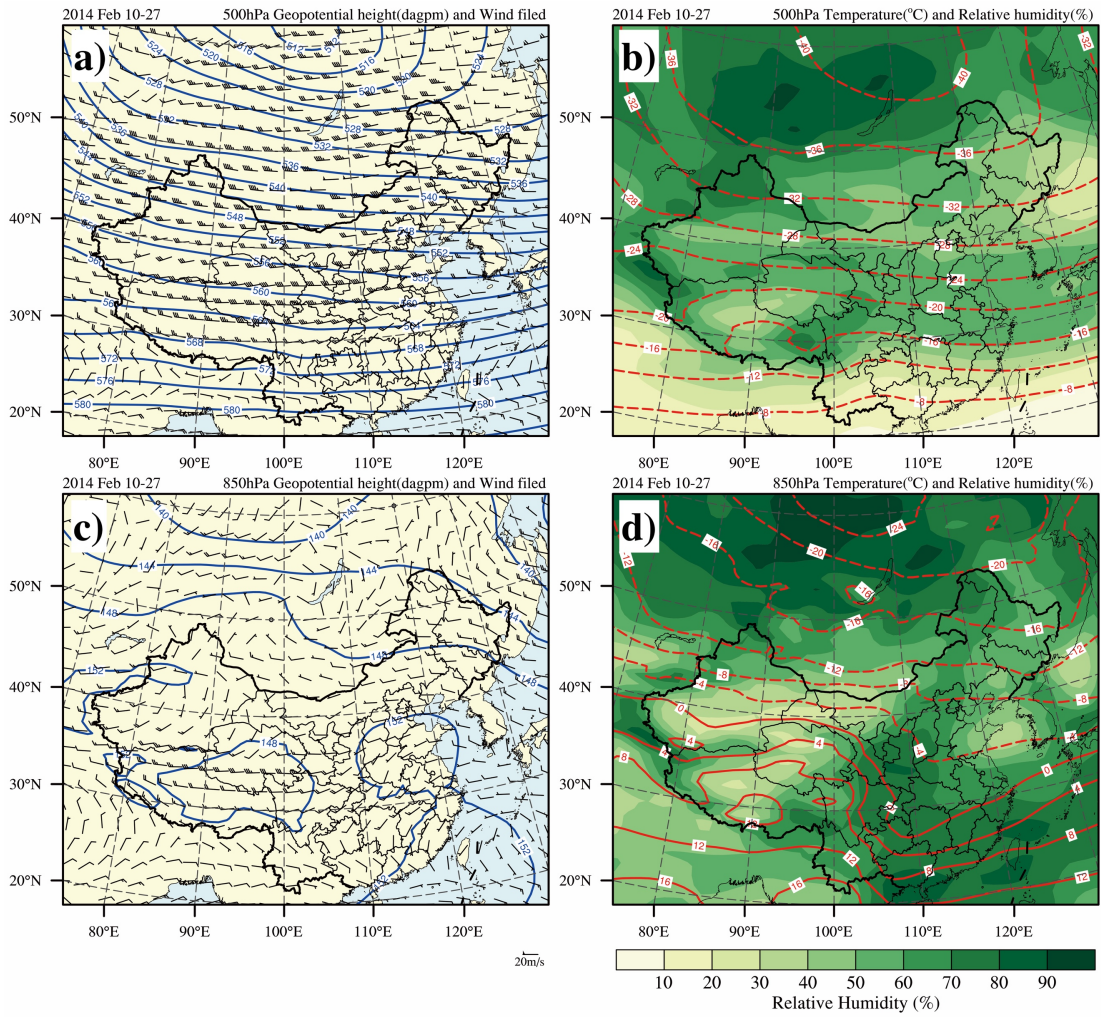
883

884

885

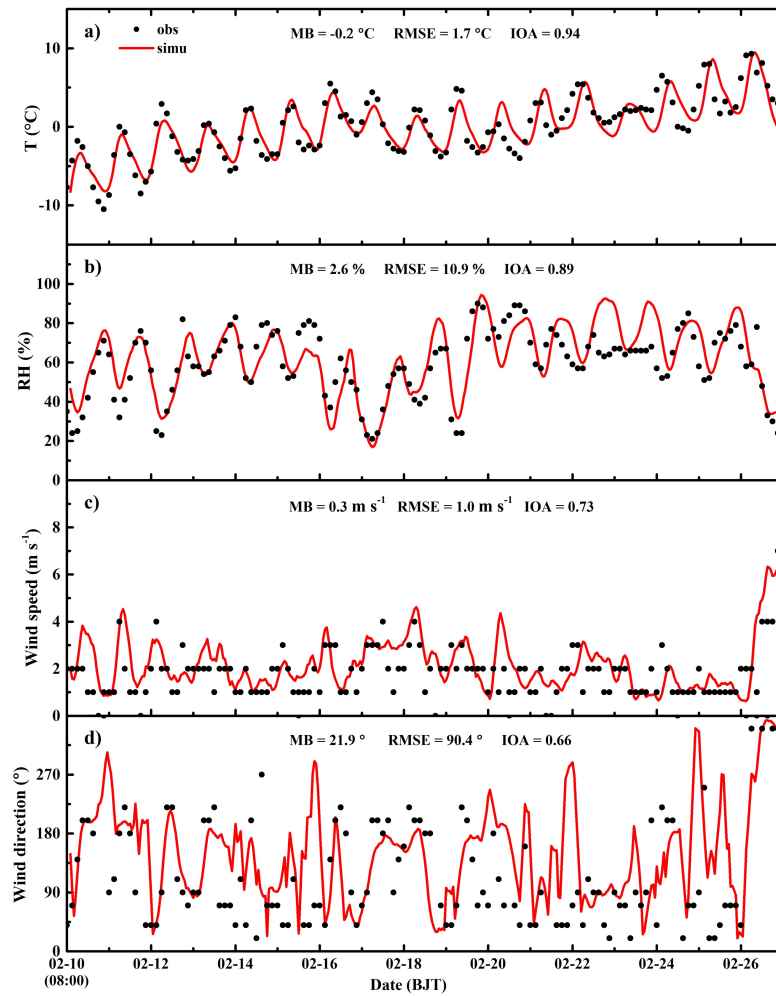
886

887



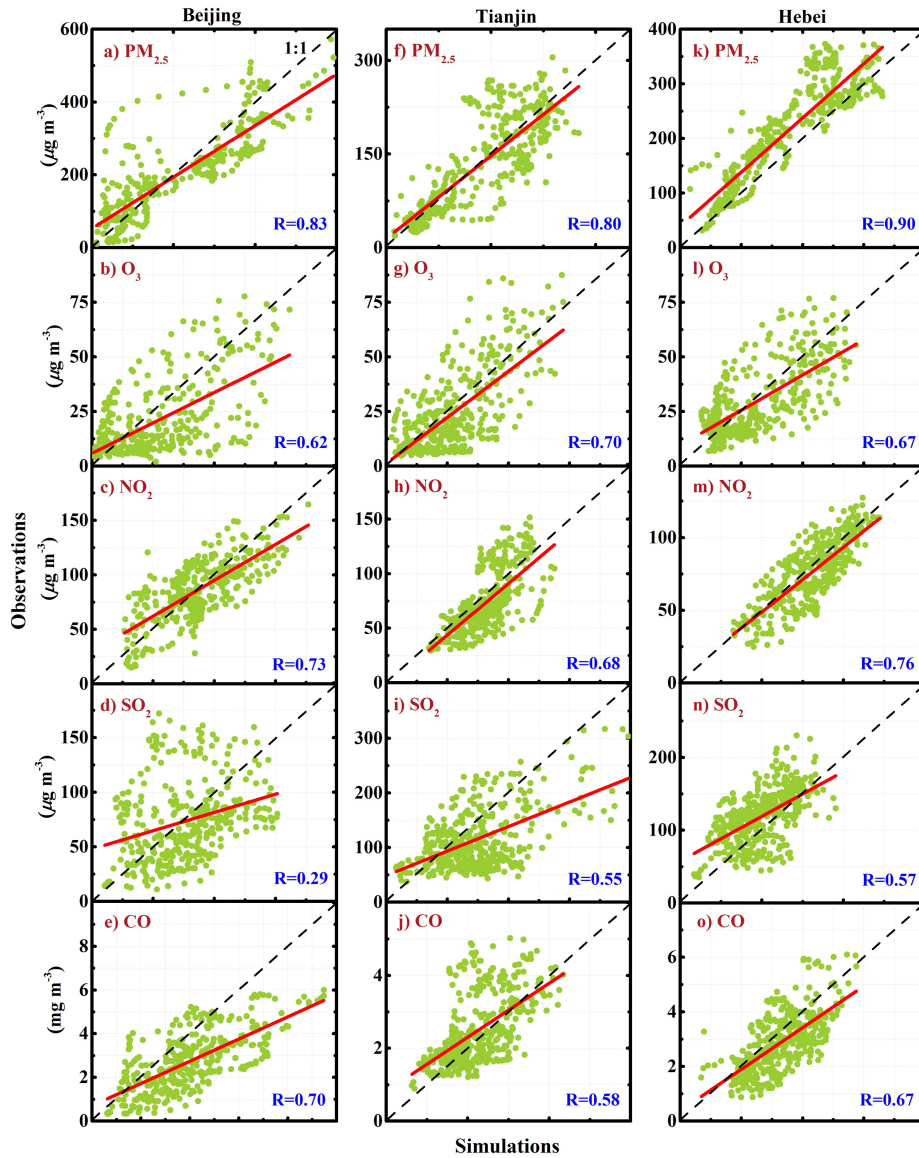
888
 889
 890
 891
 892
 893
 894
 895
 896
 897

Figure 2 Distributions of average winds (black flag vectors), geopotential heights (blue lines), temperature (red lines), and relative humidity (contour fill) at (a) and (b) 500hPa and (c) and (d) 850hPa from 10 to 27 February 2014, respectively.



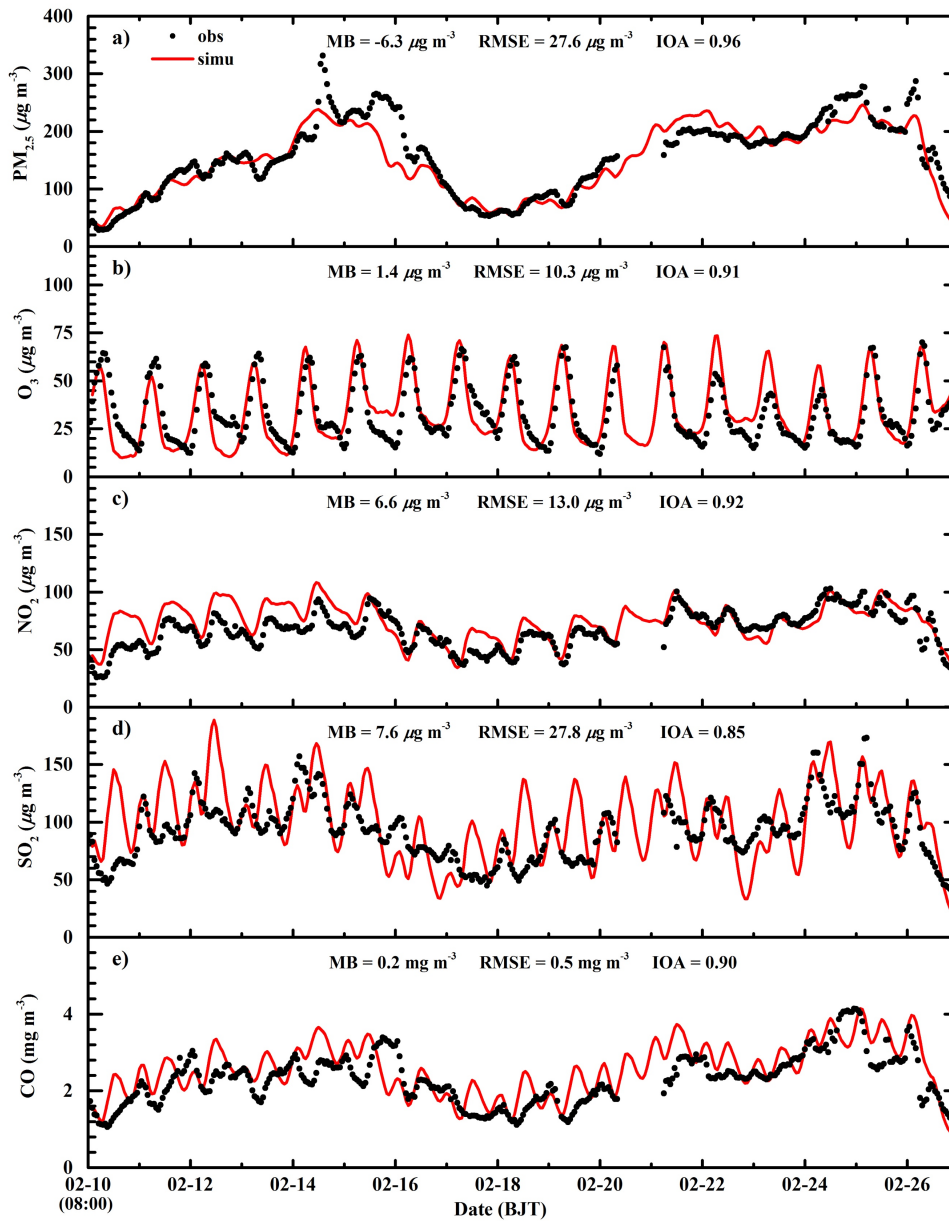
898
 899
 900
 901
 902
 903
 904
 905
 906
 907

Figure 3 Temporal variations of simulated (red line) and observed (black dots) meteorological parameters of near-surface (a) temperature, (b) relative humidity, (c) wind speed, and (d) wind direction averaged at 12 meteorological sites in Beijing from 10 to 27 February 2014.



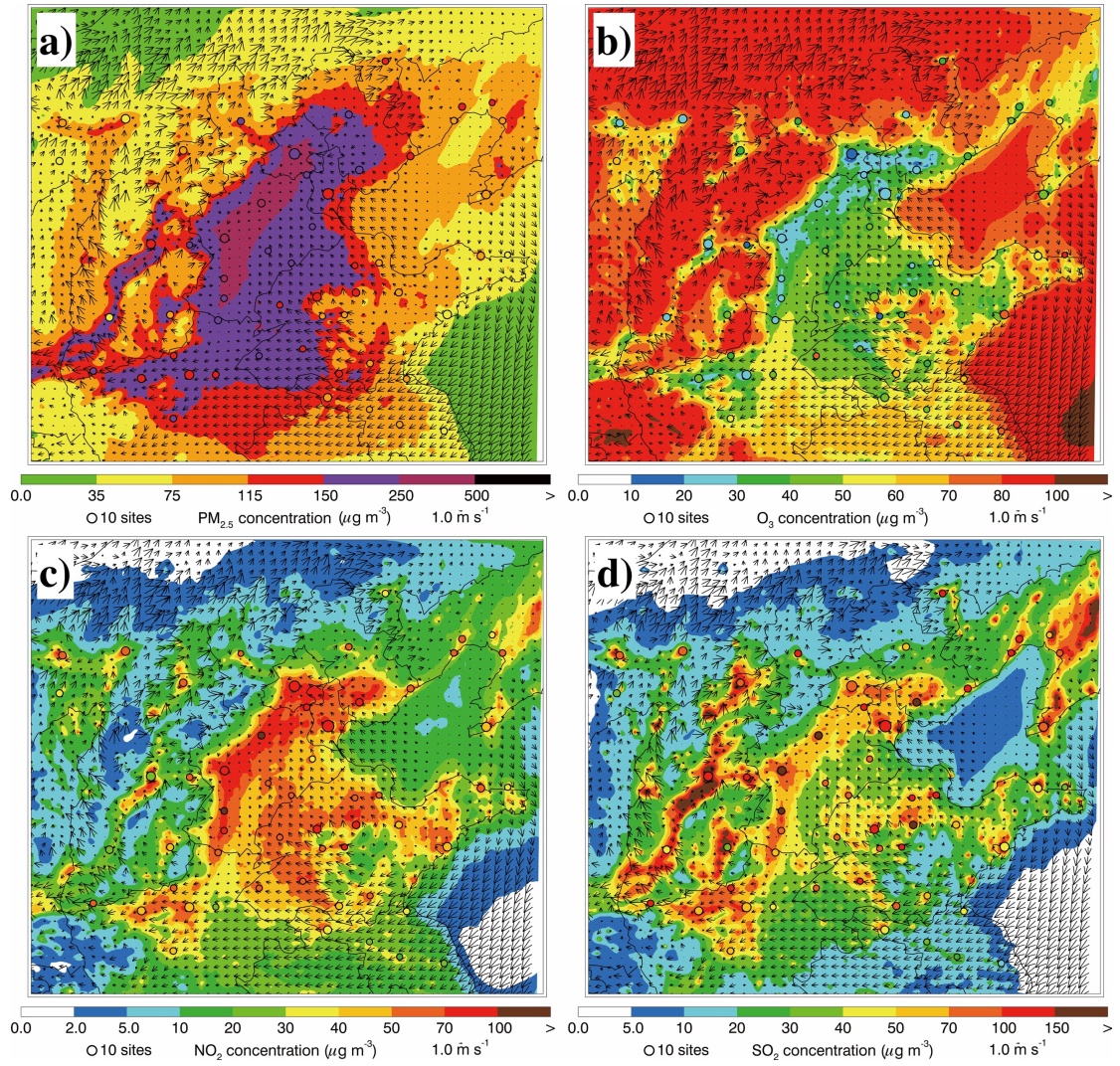
908
 909
 910
 911
 912
 913
 914
 915
 916
 917
 918

Figure 4 Relationships between observed and simulated mass concentrations of PM_{2.5}, O₃, NO₂, SO₂, and CO in Beijing, Tianjin, and Hebei from 10 to 27 February 2014. The red line is the linear regression between observations and simulations, and the black dashed line presents the 1:1 line.



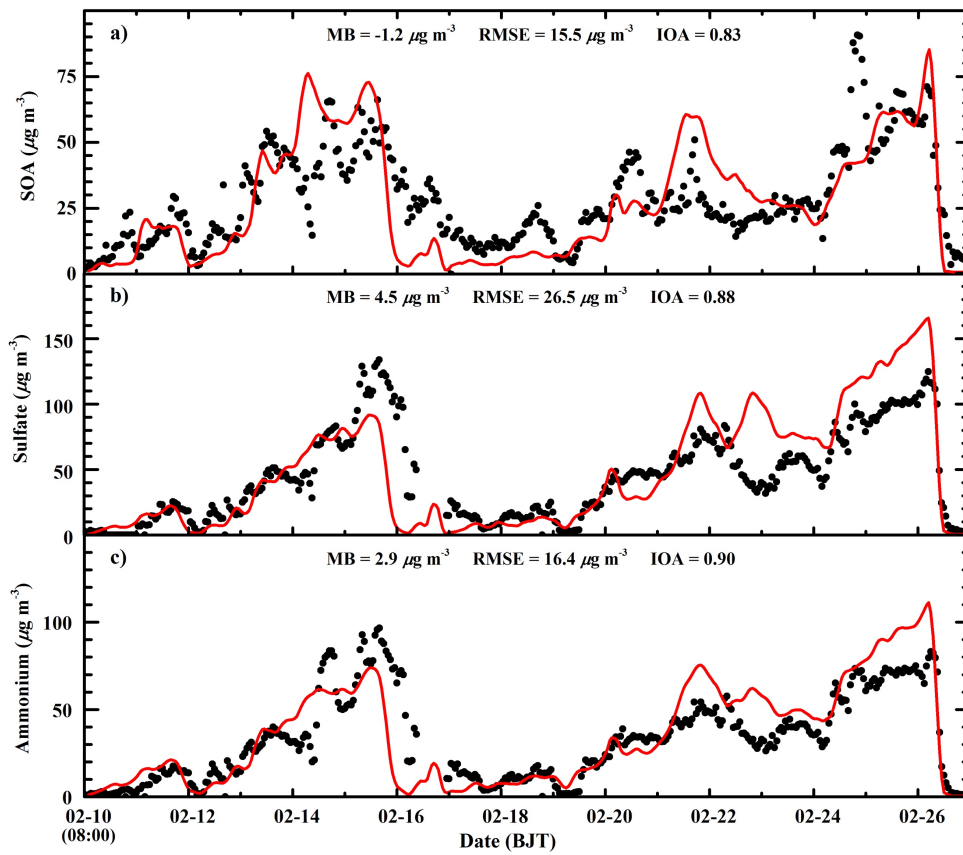
919
 920
 921
 922
 923
 924
 925
 926
 927
 928

Figure 5 Comparison of observed (black dots) and simulated (red line) diurnal profiles of near surface hourly (a) $PM_{2.5}$, (b) O_3 , (c) NO_2 , (d) SO_2 , and (e) CO averaged over all ambient monitoring stations in BTH from 10 to 27 February 2014.



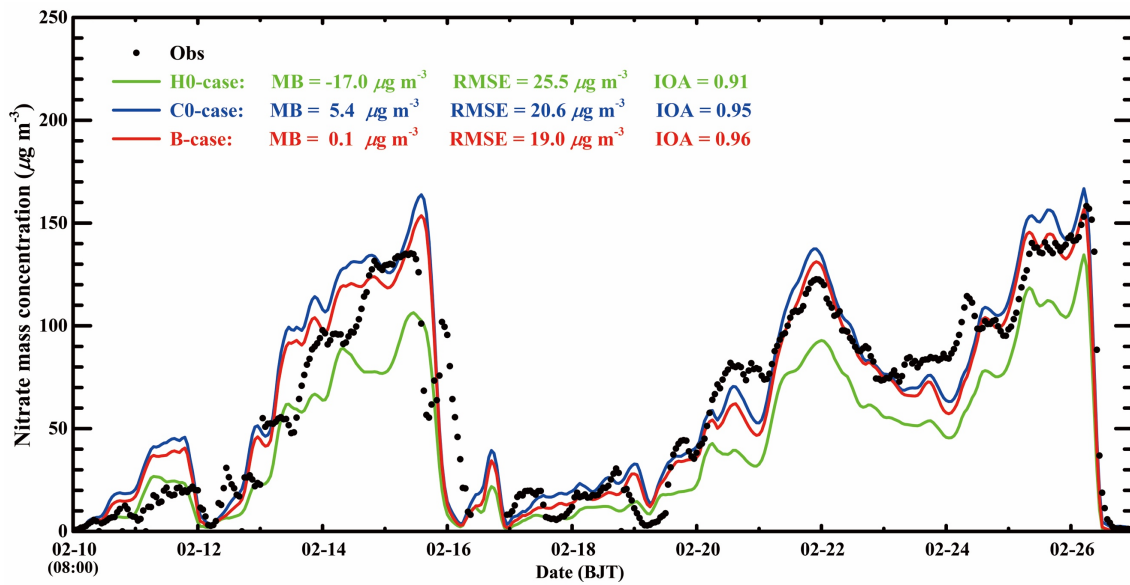
929
 930
 931
 932
 933
 934
 935
 936
 937
 938

Figure 6 Spatial distributions of average (a) PM_{2.5}, (b) O₃, (c) NO₂, and (d) SO₂ mass concentrations from 10 to 27 February 2014. Colored dots, colored contour, and black arrows are observations, simulations, and simulated surface winds, respectively.



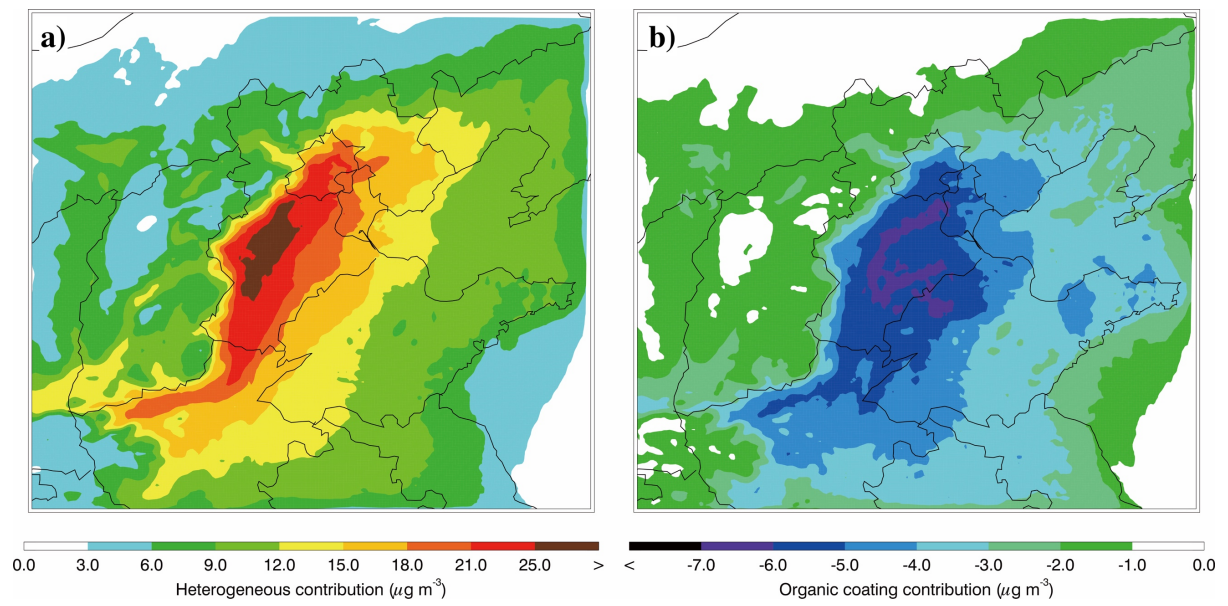
939
 940
 941
 942
 943
 944
 945
 946
 947
 948

Figure 7 Comparison of observed (black dots) and simulated (red line) diurnal profiles of hourly (a) SOA, (b) sulfate, and (c) ammonium concentrations at CRAES site in Beijing from 10 to 27 February 2014.



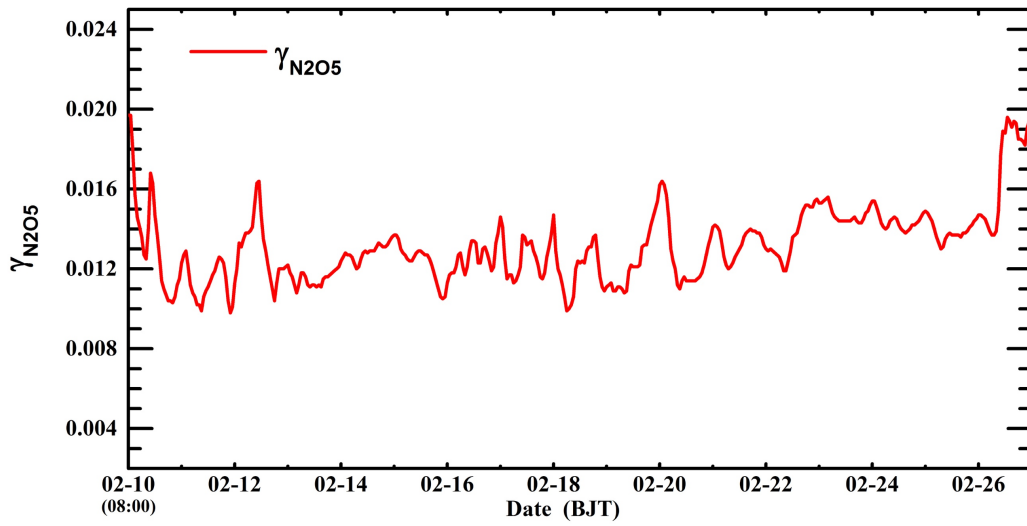
949
 950
 951
 952
 953
 954
 955
 956
 957
 958

Figure 8 Temporal variations of observed (black dot) and the simulated (Green line: H0-case; Blue line: C0-case; Red line: B-case) nitrate concentrations at CRAES site in Beijing from 10 to 27 February 2014.



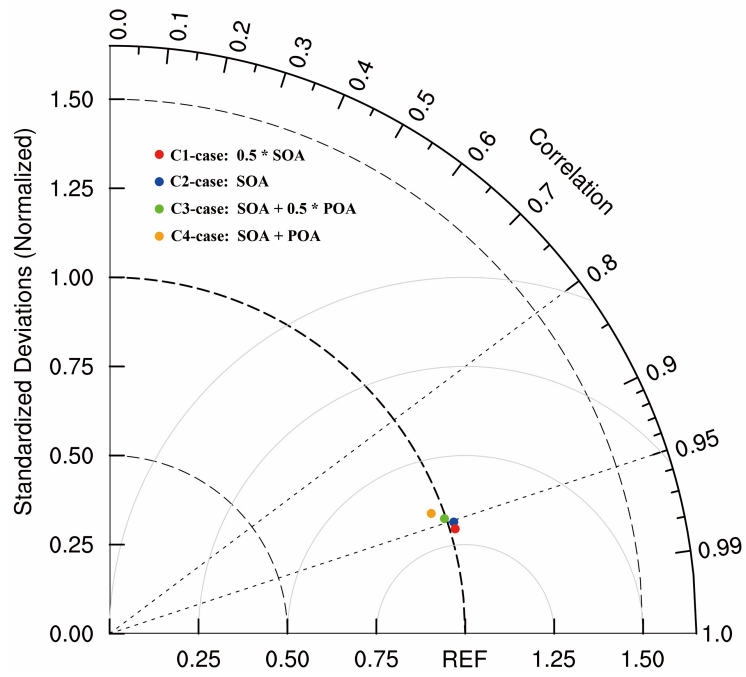
959
 960
 961
 962
 963
 964
 965
 966
 967

Figure 9 Spatial distributions of average nitrate contributions of (a) the N_2O_5 heterogeneous hydrolysis and (b) organic coating in BTH from 10 to 27 February 2014.



968
969
970
971
972
973
974
975
976

Figure 10 Temporal variation of the simulated $\gamma_{N_2O_5}$ in the B-case in Beijing from 10 to 27 February 2014.



977
 978
 979
 980
 981
 982
 983
 984
 985

Figure 11 Taylor diagram (Taylor, 2001) to present the variance, bias and correlation of the observed and simulated nitrate concentrations at CRAES site in Beijing from 10 to 27 February 2014.